Defective photoreceptor phagocytosis in a mouse model of enhanced S-cone syndrome causes progressive retinal degeneration

Debarshi Mustafi,* Brian M. Kevany,* Christel Genoud,[§] Kiichiro Okano,* Artur V. Cideciyan,[‖] Alexander Sumaroka,[‖] Alejandro J. Roman,[‖] Samuel G. Jacobson,[‖] Andreas Engel,*,[¶] Mark D. Adams,[†,‡] and Krzysztof Palczewski*,[‡,1]

*Department of Pharmacology, [†]Department of Genetics, and [‡]Center for Proteomics and Bioinformatics, Case Western Reserve University, Cleveland, Ohio, USA; [§]Electron Microscopy Facility, Friedrich Miescher Institute, Basel, Switzerland; [‖]Scheie Eye Institute, University of Pennsylvania, Philadelphia, Pennsylvania, USA; and [¶]Center for Cellular Imaging and Nanoanalytics, M.E. Müller Institute, Basel, Switzerland

ABSTRACT **Enhanced S-cone syndrome (ESCS), featuring an excess number of S cones, manifests as a progressive retinal degeneration that leads to blindness. Here, through optical imaging, we identified an abnormal interface between photoreceptors and the retinal pigment epithelium (RPE) in 9 patients with ESCS. The neural retina leucine zipper transcription factor-knockout ($Nrl^{-/-}$) mouse model demonstrates many phenotypic features of human ESCS, including unstable S-cone-positive photoreceptors. Using massively parallel RNA sequencing, we identified 6203 differentially expressed transcripts between wild-type (*Wt*) and $Nrl^{-/-}$ mouse retinas, with 6 highly significant differentially expressed genes of the Pax, Notch, and Wnt canonical pathways. Changes were also obvious in expression of 30 genes involved in the visual cycle and 3 key genes in photoreceptor phagocytosis. Novel high-resolution (100 nm) imaging and reconstruction of $Nrl^{-/-}$ retinas revealed an abnormal packing of photoreceptors that contributed to buildup of photoreceptor deposits. Furthermore, lack of phagosomes in the RPE layer of $Nrl^{-/-}$ retina revealed impairment in phagocytosis. Cultured RPE cells from *Wt* and $Nrl^{-/-}$ mice illustrated that the phagocytotic defect was attributable to the aberrant interface between ESCS photoreceptors and the RPE. Overcoming the retinal phagocytosis defect could arrest the progressive degenerative component of this disease.—Mustafi, D., Kevany, B. M., Genoud, C., Okano, K., Cideciyan, A. V., Sumaroka, A., Roman, A. J., Jacobson, S. G. Engel, A., Adams, M. D., Palczewski, K. Defective photoreceptor phagocytosis in a mouse model of enhanced S-cone syndrome causes progressive retinal degeneration. *FASEB J.* 25, 3157–3176 (2011). www.fasebj.org**

Key Words: Nrl · RNA-Seq · vision

The retina of all vertebrates contains rod photoreceptors for dim light environments and cone photoreceptors for brighter environments; cones are further divided into short-wavelength-sensitive (S) and long- and middle-wavelength-sensitive (L/M) subtypes. These photoreceptors, which are organized into mosaic structures with characteristic rod/cone ratio in retinal position and species specific manner, are organized to provide useful visual sensation for the animals during their entire life span. Thus, a normal retina is controlled by a multitude of interacting factors that determine the precise developmental organization and lifetime maintenance of interconnected neurons for optimal visual function (1, 2). Disruption of these complex interactions during development or in the mature retina can give rise to cellular pathology, mainly manifesting as loss of vision. In addition to the development and maintenance processes of the photoreceptor itself, homeostatic processes in neighboring cells contribute to photoreceptor health. A key example of this support function is continuous phagocytosis of shed photoreceptor discs by the neighboring retinal pigment epithelium (RPE; refs. 3–5).

Enhanced S-cone syndrome (ESCS) is a human visual disorder first recognized for its unique feature of showing increased S-cone vision. With noninvasive studies, ESCS was demonstrated to result in supernormal sensitivity to blue colors and an excess number of S cones, normally the minority photoreceptor in the human retinal mosaic consisting mainly of rods and L/M cones. In contrast, rod and L/M-cone vision are reduced in ESCS. A hypothesis emerging from these results was that abnormal retinal development causes ESCS involving a disturbance in photoreceptor cell specification (6–8). A search for the causative genes

[1] Correspondence: Department of Pharmacology, School of Medicine, Case Western Reserve University, 10900 Euclid Ave., Cleveland, Ohio 44106-4965, USA. E-mail: kxp65@case.edu

doi: 10.1096/fj.11-186767

This article includes supplemental data. Please visit *http://www.fasebj.org* to obtain this information.

ensued, and mutations in most patients mapped to the gene encoding the human photoreceptor-specific nuclear receptor, *NR2E3*, while a few mapped to the neural retina leucine zipper, *NRL*, gene (9–11). *NR2E3* and *NRL* are now known to play key roles in the regulatory transcriptional networks controlling photoreceptor cell fate (1). Identification of the causative genes, however, did not account for the degenerative component of this disease.

Knockout of the *Nrl* transcription factor in mice produces a retina overpopulated with S-cone-like photoreceptors along with absence of rod photoreceptors. Precise identification of changes in transcriptional networks in the $Nrl^{-/-}$ mouse retina and resulting aberrant composition of expressed proteins would likely provide information concerning critical factors that dictate cone-like photoreceptor maintenance/survival as well as proper retinal lamination. Previous studies have also suggested abnormal association between photoreceptors and the RPE in $Nrl^{-/-}$ mice (12, 13), and differences in RPE appearance such as discontinuity and depigmentation compared with normal RPE have been noted in human postmortem donor ESCS retinas (14, 15). Our own electron microscopy (EM) revealed aberrant bulbous outer segment (OS) structures containing abnormal internal structures (16).

Early stages of photoreceptor development and maintenance involve Notch signaling through basic helix loop helix (bHLH) transcription factors (17, 18), as well as through Hedgehog, which also converges on downstream Notch targets (19). The interplay of these factors, among others, dictates the proper transcriptional environment for photoreceptor maintenance, but the precise relationship between them is not yet fully elucidated. Previous studies of the retinal tissue transcriptome in mouse models employed microarray-based serial analysis of gene expression (SAGE; refs. 20–23), expressed sequence tag (EST; refs. 24, 25), and hybridization microarrays (26–28), but a complete transcriptome analysis could not be achieved by these approaches. Recent developments have revolutionized transcriptome analysis. RNA-sequencing (RNA-Seq) technology now combines the advantages of previous large-scale RNA analytical methods with a larger dynamic range of detection (29, 30), and already has provided new genetic insights in different model systems (31–33).

We now report RNA-Seq transcriptome analyses and quantification of transcript levels to identify genes differentially expressed in mature wild-type (*Wt*) and $Nrl^{-/-}$ mouse eyes and retinas. We identified changes in expression of the set of genes involved in the formation/maintenance of cone-like photoreceptors of the $Nrl^{-/-}$ retina and noted changes in key homeostatic genes involved in OS disc phagocytosis and toxic metabolite removal that suggested a potential molecular mechanism for the degenerative component of ESCS. The genetic findings were complemented by a set of new imaging technologies (34, 35) used to assess the disrupted retinal layering in $Nrl^{-/-}$ mice, the abnormal photoreceptor-RPE interface, and the process of phagocytosis (3). Imaging and biochemical experiments revealed fewer detectable phagosomes in $Nrl^{-/-}$ *as* compared to *Wt* retina. Compromised phagocytosis was attributed to a defect in the aberrant $Nrl^{-/-}$ photoreceptors rather than phagocytes because RPE cell cultures from $Nrl^{-/-}$ retina exhibited phagocytosis comparable to RPE cell cultures from *Wt* animals. These results are consistent with the hypothesis that impairment in phagocytosis stemming from aberrant ESCS photoreceptors leads to retinal degeneration in both patients with ESCS and the $Nrl^{-/-}$ mouse model.

MATERIALS AND METHODS

Materials

All chemicals, unless otherwise stated, were purchased from Sigma-Aldrich (St. Louis, MO, USA). Reagents for cDNA library preparation for Illumina sequencing, unless otherwise indicated, were bought from Illumina (San Diego, CA, USA). Reagents for cDNA synthesis and quantitative real-time PCR (RT-PCR) were obtained from Applied Biosystems (Foster City, CA, USA). Primary antibodies anti-red/green pigment opsin and anti-blue opsin were acquired from Chemicon International (Billerica, MA, USA), anti-phosphatidylserine (PS) and anti-annexin V were purchased from Abcam (Cambridge, MA, USA), peanut aggulutinin (PNA) was obtained from Invitrogen (Carlsbad, CA, USA), and anti-rhodopsin was generated in the K.P. laboratory from hybridoma cells (36). Cy3 and Alexa488 conjugated secondary antibodies were acquired from Jackson Immuno-Research (West Grove, PA, USA) or Invitrogen. Nuclear staining was achieved with Hoechst, 4′,6-diamidino-2-phenylindole (DAPI), or quinolinium, 4-[3-(3-methyl-2(3H)-benzothiazolylidene)-1-propenyl]-1-[3-(trimethylammonio)propyl]-diiodide (ToPro3; Invitrogen).

Human studies

All patients with ESCS studied had mutations in the *NR2E3* gene (11). Informed consent was obtained, and procedures followed the Declaration of Helsinki guidelines and were approved by the institutional review board at the University of Pennsylvania. Patients had complete ocular examinations including kinetic perimetry quantified by published methods (37). Psychophysical thresholds were measured with a modified automated perimeter (Humphrey Field Analyzer; Humphrey Instruments, San Leandro, CA, USA) to determine S-cone function (440-nm stimulus on a yellow background, 170 cd/m^2), L/M cone function (650-nm stimuli, dark-adapted) and rod function (500-nm stimuli, dark-adapted). Details of visual function techniques and analyses have been described previously (6, 7, 15). Spectral-domain (SD) optical coherence tomography (OCT) was used (RTVue-100; Optovue Inc., Fremont, CA, USA) with published recording and analysis techniques to perform retinal cross-sectional imaging (38–41). RPE lipofuscin imaging was performed as described previously (38, 42).

Animals

Mice were housed in the animal facility at the School of Medicine, Case Western Reserve University (CWRU; Cleveland, OH, USA), where they were maintained on a standard

chow diet in a 12-h light-dark cycle (light ~10 lux). *Wt* mice on C57BL/6 background were obtained from The Jackson Laboratory (Bar Harbor, ME, USA). *Nrl*-deficient mice in the C57BL/6 background were from Dr. Anand Swaroop (University of Michigan, Ann Arbor, MI, USA; ref. 12). Genotyping of mice was done by PCR with primers NRL-A (5′-gtgttccttggctggaaaga-3′) and NRL-B (5′-ctgttcactgtgggctttca-3′) for *Wt* and NRL-KO1 (5′-tgaatacagggacgacacca-3′) and NRL-KO2 (5′-gttctaattccatcagaagctgac-3′) for targeted deletion of the *Nrl* gene. All animal procedures and experiments were performed in accordance with U.S. animal protection laws and were approved by the CWRU Animal Care Committees and conformed to both the recommendations of the American Veterinary Medical Association Panel on Euthanasia and the Association of Research for Vision and Ophthalmology.

Ultra-high-resolution SD-OCT

Nine *Wt* and 9 *Nrl*-deficient mice aged 4 wk were each anesthetized by intraperitoneal injection of a mixture (20 μl/g body weight) containing ketamine (6 mg/ml) and xylazine (0.44 mg/ml) in 10 mM sodium phosphate (pH 7.2) and 100 mM NaCl. Pupils were dilated with 1% tropicamide. Mice were placed in a specialized holder to permit ultra-high-resolution SD-OCT (Bioptigen, Research Triangle Park, NC, USA) for *in vivo* imaging of mouse retinas at $\lambda = 870$ nm with a superluminescent diode. Each 2-dimensional (2-D) B scan was acquired at a speed of 1000 scans/s, and each final SD-OCT image was an average of 3 individual B-scans. Three-dimensional (3-D) scans were taken around the optic nerve with a scanning radius of 1.6 mm. Images were postprocessed by using commercial Bioptigen software and ImageJ (U.S. National Institutes of Health, Bethesda, MD, USA) (43).

Library preparation for sequencing

Mice were euthanized by cervical dislocation. Eyes were enucleated and immediately placed in RNA later stabilization reagent (Qiagen, Valencia, CA, USA) to preserve RNA content and integrity (44) for whole-eye runs. Alternatively, the retina was rapidly dissected out and similarly preserved. One mouse eye or 2 retinas were homogenized at once and passed through a QIAShredder column (Qiagen) as per manufacturer's directions to further homogenize the eye tissues. Total RNA was then purified by using the RNeasy Mini Kit (Qiagen) with on column DNase treatment (Qiagen) as per manufacturer's directions. Poly(A) RNA was isolated with the Oligotex kit (Qiagen) as per the manufacturer's instructions. Pooled total RNA samples of 5 *Wt* and 5 $Nrl^{-/-}$ female mice at 4 wk of age were used for the whole-eye library preparation, and pooled total RNA samples from 5 *Wt* and 5 $Nrl^{-/-}$ female mice at 4 wk of age were used for the retina library preparation.

For first-strand cDNA synthesis, instructions from the SuperScript III kit protocol (Invitrogen) were followed. About 400–450 ng of isolated poly(A) RNA was mixed with 50 ng of random primers and 1 mM deoxyribonucleotide triphosphate (dNTP), incubated at 65°C for 5 min, and then placed on ice for 5 min. A reaction mixture comprising 5 mM $MgCl_2$, 10 mM DTT, 40 U RNaseOUT, and 200 U SuperScript III reverse transcriptase was added to the initial mix to achieve a total volume of 20 μl. The mixture was incubated at 25°C for 10 min, followed by 50 min at 50°C. The reaction was terminated at 85°C for 5 min and then chilled on ice for 10 min. At this point, 2 U RNase H was added, and the mix was incubated at 37°C for 20 min. The first-strand cDNA synthesis reaction was immediately used for second-strand synthesis. To the first-strand product, 300 μM dNTP, *Escherichia coli* DNA polymerase I buffer, and water were added to obtain a total volume of 95 μl and allowed to incubate on ice for 10 min. Then, 0.05 U *E. coli* DNA polymerase I (New England Biolabs, Beverly, MA, USA) was added, and the mixture was incubated at 16°C for 2.5 h. The resulting double-stranded cDNA was purified with the Wizard SV Gel and PCR Clean-up System (Promega, Madison, WI, USA), eluted in 100 μl nuclease-free water, and then fragmented by the Covaris S2 instrument (Covaris, Woburn, MA, USA) to generate ~200-bp fragments as follows: 10% duty cycle, intensity of 5, 100 cycles/burst, with a bath temperature of 7.7°C and an acoustic power of 24 W.

The Illumina library was prepared according to the manufacturer's instructions and purified using the Wizard SV Gel and PCR Clean-up system. Overhangs were converted into blunt ends with T4 DNA polymerase and Klenow DNA polymerase by incubating the mixed sample at 20°C for 30 min. cDNA was purified and eluted in 32 μl of nuclease-free water with the Wizard Plus Minipreps DNA purification system (Promega). The purified sample was then mixed with Klenow fragment (3′ to 5′ exo minus) and incubated at 37°C for 30 min to add an A base to the 3′ end of the blunt phosphorylated DNA fragments. The cDNA was then purified and eluted in 23 μl of nuclease-free water with the Wizard Plus Minipreps system. Eluted DNA was mixed with Illumina Adapter Oligo mix and T4 DNA ligase and incubated at room temperature for 15 min to ligate adapters to the ends of the DNA fragments to prepare them for hybridization to the flow cell. cDNA then was purified and eluted in 10 μl of nuclease-free water with the Wizard Plus Minipreps system (Promega). cDNA templates were purified by running samples on a 1% agarose gel at 120 V for 60 min and excising the region of the gel in the 200-bp range. The 200-bp cDNA enriched fragments were purified and eluted in 30 μl of nuclease-free water with the Wizard Plus Minipreps system. cDNA in the library was then amplified by a 15 cycle PCR with two primers that annealed to the ends of the adapters. The amplified cDNA was purified and eluted in 30 μl of nuclease-free water with the Wizard Plus Minipreps system. The size, purity and concentration of the final library was checked with the Bio-Rad Experion DNA specific chip prior to sequencing by using the Illumina Genome Analyzer. The concentration of the sample was also measured using 1 μl of purified sample with the Qubit Quantitation Platform (Invitrogen) to estimate loading conditions for the Illumina Cluster Station.

Genome analyzer RNA-Seq runs, read mapping, and quantification

Each library was run on 3 lanes of the Genome Analyzer II in the Genomics Core Facility at CWRU by using 36- or 49-bp single-end sequencing. The numbers of mapped single reads from different experiments were 38,166,142 from the whole-eye technical replicates; 45,431,330 from the *Wt* whole eye; 66,643,381 from the $Nrl^{-/-}$ eye; 85,159,191 from the *Wt* retina; and 104,081,398 from the $Nrl^{-/-}$ retina. Technical replicates of the whole eye entailed running the sample library preparation on independent lanes on different day runs and analyzing them separately. Primary data transformation included image analysis, intensity scoring, base calling, and alignment, all carried out with Illumina pipeline software running on Linux. Image analysis identified distinct clusters and created digital intensity files describing the signal intensity of each cluster per cycle. Signal intensity profiles for each cluster were used to call bases, and quality scores for each base call were calculated for alignment. Efficient Large-Scale Alignment of Nucleotide Databases (ELAND; Illumina) was then used for read mapping to the University of California–Santa Cruz (UCSC; Santa Cruz, CA, USA) mouse genome

assembly and transcript annotation (mm9) (45). For each read, ELAND determined the position in the genome to which the read substrings matched with a maximum of 2 errors. Base quality scores and the positions of the mismatches in a candidate alignment were used to calculate a probability score for each candidate, with the highest probability score indicating the best candidate. Eligible reads were defined by having a unique alignment to the genome or a single most probable alignment to the genome. Other reads with failed quality control measures were not used in subsequent processing. The ELAND alignment was loaded onto Consensus Assessment of Sequence and Variation (CASAVA; Illumina) software for calculation of fragments per kilobase of exon model per million mapped reads (FPKM) statistics by gene, transcript, and exon. CASAVA counted the number of bases that belonged to exons and genes, and the numbers of bases that fell into the exonic regions of each gene were summed to obtain gene level counts. Normalized values were then calculated as FPKM. The output for CASAVA was visualized with the GenomeStudio RNA Sequencing Module (Illumina), which allowed comparison between the samples based on the CASAVA output files. The raw files (fastq) and processed FPKM value data can be found online at the National Center for Biotechnology Information gene expression omnibus site with the series accession number GSE29752 (http://www.ncbi.nlm.nih.gov/projects/geo/query/acc.cgi?acc=GSE29752).

RT-PCR

Isolated total retinal RNA (2 μg) from 3 pooled *Wt* and *Nrl*$^{-/-}$ samples was converted to cDNA with the High Capacity RNA-to-cDNA kit (Applied Biosystems). RT-PCR was done with TaqMan chemistry and Assays on Demand probes (Applied Biosystems) for mouse *Abca4* (Mm00492035_m1), *Atp8a2* (Mm00443740_m1), *Atoh7* (Mm00844064_s1), *Bmp15* (Mm00437797_m1), *Crx* (Mm00483995_m1), *Egr1* (Mm00656724_m1), *Eya1* (Mm00438796_m1), *Gdf11* (Mm01159973_m1), *Neurod1* (Mm01946604_s1), *Notch1* (Mm00435249_m1), *Prdm1* (Mm01187284_m1), *Opn1sw* (Mm00432058_m1), *Otx2* (Mm00446859_m1), *Six6* (Mm00488257_m1), *Six6os1* (Mm01290652_m1), *Thrb* (Mm00437044_m1), *Rxrg* (Mm00436411_m1), and *Wnt9b* (Mm00457102_m1). The 18S rRNA (4319413E) probe set (Applied Biosystems) was used as the endogenous control. All real-time experiments were done in triplicate with the ABI Step-One Plus qRT-PCR machine (Applied Biosystems). Fold changes were calculated based on differences in threshold cycles (C_t) between the *Nrl*$^{-/-}$ and *Wt* samples after normalization to 18s rRNA.

Analysis of data

Genes were categorized using AmiGO 1.8 software (http://www.geneontology.org/). Fold differences in RNA-Seq experiments were compared by examining the ratio of FPKM between *Wt* and *Nrl*$^{-/-}$ sample runs. A 1.5-fold or greater change in threshold was used to identify differential expression, thereby allowing comparisons with previous experiments. Statistical significance of fold expression changes in RT-PCR were analyzed with Microsoft Excel software (Microsoft, Redmond, WA, USA). *P* values were calculated from a Student's 2-tailed *t* test to confirm that fold changes were statistically significant ($P<0.05$). Power analysis was calculated to detect the sample size required to detect significant changes with RNA-Seq using a 1.5-fold difference cutoff. The parameters were detecting a 0.33=FPKM difference (a 1.5-decreased fold of 1 FPKM, representing an expressed transcript, is 0.67, yielding a difference of 0.33 FPKM), a standard deviation of 10% in the FPKM value (estimated from technical replicates), an α value of 0.05, and a β value of 0.10, with the ratio of *Wt* to *Nrl*$^{-/-}$ samples as 1.

Cryosectioning

Twenty *Wt* and 20 *Nrl*-deficient mice aged 4 wk were sacrificed 1.5 h after lights went on in the morning, a time when phagocytosis of photoreceptor OS in *Wt* is maximal. Eye cups were dissected out under a surgical microscope and incubated in 4% paraformaldehyde overnight at 4°C. Eye cups then were dehydrated in successive solutions of 5, 10, 15, and 20% sucrose in phosphate buffered saline (PBS; 137 mM NaCl, 2.7 mM KCl, 4.3 mM Na_3HPO_4, and 1.4 mM KH_2PO_4, pH 7.3) for 30 min each on a shaker. Subsequently, eyes were placed in a 1:1 solution of 20% sucrose in PBS:Optical Cutting Temperature Compound (Tissue-Tek-Sakura, Torrence, CA, USA) for 30 min on a shaker, when the solution was replaced and the eye cups were kept at 4°C overnight. Eye cups were frozen the next day by placing them in cryomolds and submerging them into 2-methyl-butane in a tank of liquid nitrogen. Cryoblocks were then cut with a Leica cryosectioner (Leica Microsystems, Wetzlar, Germany) and 10-μm sections around the optic nerve were collected on glass slides for immunohistochemical staining.

Immunohistochemistry

All procedures used were reported previously (46, 47). Cross-sections of mouse eyecups were incubated with primary antibodies, namely anti-rabbit red/green pigment opsin, anti-rabbit opsin blue anti-mouse rhodopsin, anti-mouse PS, anti-rabbit annexin V, and PNA. Signals were detected with either Cy3-conjugated secondary antibody or Alexa488-conjugated secondary antibody. Nuclear staining was achieved with DAPI. Sections were analyzed with a Leica 6000B microscope.

Whole-mount retinal confocal microscopy

Ten *Wt* and 10 *Nrl*-deficient 4-wk-old mice were sacrificed, and eye whole mounts were prepared and incubated overnight with primary antibodies; *i.e.*, anti-rabbit red/green pigment opsin, anti-rabbit opsin blue anti-mouse rhodopsin, anti-mouse PS, and PNA. Signals were detected with either Cy3-conjugated secondary antibody or Alexa488-conjugated secondary antibody. Nuclear staining was achieved with To-Pro3. Thick *Z* stacks (30–40 μm) were collected at ×40 view with 1 μm between each slice and visualized with a Leica SP5 confocal microscope. Obtained images were postprocessed with ImageJ to adjust contrast and brightness.

Scanning EM (SEM)

Seven *Wt* and 9 *Nrl*-deficient mice 4 wk of age were sacrificed, and their retinas and the RPE were separated and fixed in 2.5% glutaraldehyde, 0.1 M cacodylate buffer, and 2% sucrose (pH 7.4) for 24 h. Samples were washed in 0.1 M cacodylate buffer and 2% sucrose, fixed with 1% OsO_4 in washing buffer, dehydrated with ethanol, dried by a critical point drying method (48), and sputter-coated with a 5–10 nm gold layer. Samples were imaged with a JSF-6300F scanning electron microscope (Jeol, Akishima, Japan) at the University of Washington Department of Pathology (Seattle, WA, USA). The emission current was set to enable acquisition of back-scattered electron scanning images at ×2000 to ×10,000.

Transmission EM (TEM)

Five *Wt* and 5 *Nrl*-deficient mice aged 4 wk and 5 *Wt* and 5 *Nrl*-deficient mice aged 8 wk were sacrificed at 1.5 h after lights went on in the morning. Eyes were removed, and whole eye cups were dissected out under a surgical microscope and placed in 4% paraformaldehyde at 37°C for 4 h. Eye cups then were rinsed in PBS and incubated in a 1:1 solution of 2% OsO_4:3% potassium ferrocyanide for 1 h. This was followed by incubation in a new mixture of 2% OsO_4:3% potassium ferrocyanide for 1 h, after which eye cups were washed in filtered water and placed in 0.25% uranyl acetate overnight at 4°C. Eye cups were dehydrated the next day for 10 min each in sequential solutions of 30, 50, 75, 85, 95, and 100% ethanol in water, then for 15 min each in sequential solutions of 50, 75, and 100% propylene oxide in ethanol, followed by 2 h in 30% epon in propylene oxide, and finally kept in 50% epon in propylene oxide overnight. Next day, eye cups were placed in 75% epon in propylene oxide for 4 h, then in 100% epon for 2 h under vacuum, and finally in a mold with epon kept at 73°C for 4 d to enable cross-linking. Then blocks were cut with a microtome, and ultrathin sections (0.07 μm) were stained with uranyl acetate and adsorbed onto carbon grids. A Tecnai T12 electron microscope (FEI, Eindhoven, Netherlands) operating at 120 kV with a tungsten filament was used for final imaging.

Serial block face SEM (SBF-SEM), SEM data analyses, and 3-D reconstruction

The same blocks prepared for TEM were used for SBF-SEM (34). To prepare a sample, we used an ultramicrotome (Leica UCT) and a diamond knife (Diatome, Hatfield, PA, USA), and trimmed the block so that only resin-embedded tissue of the region of interest remained. The final tissue block was adhered by conductive carbon cement to an aluminum SEM stub to preserve conductivity. The prepared sample was fixed on the microtome (3View; Gatan, Pleasanton, CA, USA) attached on the door of the scanning electron microscope (Quanta 200 FEG ESEM; FEI). Cutting was initiated in the evacuated specimen chamber. To perform serial cutting of the block face, a 100-nm slice was cut from the face with a diamond knife, and the freshly cut surface of the block was imaged from the backscattered electron signal. This process was repeated sequentially in an automatic computer-controlled fashion to collect 500 successive images over ~12 h. Imaging was performed at an accelerating voltage of 3 kV in a low-vacuum mode (0.23 Torr) at 4096- × 4096-pixel resolution at a rate of 3 μs/pixel.

After serial sectioning, images were opened with Fiji-win32 (a version of ImageJ; http://imagej.nih.gov/ij/index.html) and merged to form a stack. The stack was registered and aligned to account for any drift that may have occurred over the time course of sectioning. The registered stack then was opened using the Reconstruct program (49), and structural elements were mapped to provide 3-D reconstructions.

Phagocytosis assays of RPE cell cultures

RPE was isolated from 10- to 12-d-old *Wt* and $Nrl^{-/-}$ mice as described previously (50). Briefly, eyes were removed from animals and washed twice in Dulbecco's modified Eagle's medium (DMEM; Invitrogen) supplemented with nonessential amino acids. Eyes were incubated in 2% dispase (Invitrogen) solution for 45 min in a 37°C water bath with occasional tube inversion. Eyes were washed twice in cold DMEM plus streptomycin/penicillin (Invitrogen), 10% fetal bovine serum (Invitrogen), and 20 mM HEPES (pH 7.2). Eyes were enucleated, and the cornea, lens, and iris were removed. Eye cups were incubated in DMEM plus streptomycin/penicillin, 10% fetal bovine serum, and 20 mM HEPES (pH 7.2) in a 37°C incubator for 15 min to facilitate removal of the neural retina. After removal of neural retina, sheets of continuous RPE were peeled from choroid and pipetted into a tube containing DMEM plus streptomycin/penicillin and 10% fetal bovine serum. RPE sheets were subsequently filtered over a 40-μm cell strainer (Fisher Scientific, Pittsburgh, PA, USA) to remove contaminating cell types. Sheets were spun at 200 *g* for 3 min and then resuspended in DMEM plus streptomycin/penicillin and 10% fetal bovine serum before gentle disruption by pipetting. Disrupted cells were seeded onto 24-well 0.4-μm transwell permeable supports (Corning Inc., Corning, NY, USA) with the RPE from ~2 eyes/well to allow polarization of cells. Cells were grown for 5–6 d at 37°C, 5% CO_2 before use in phagocytosis assays.

For phagocytosis challenge assays, photoreceptor OS membranes were isolated from *Wt* and $Nrl^{-/-}$ mice. Photoreceptor OS membranes from *Wt* mice were isolated as described previously (51), whereas OS membranes from $Nrl^{-/-}$ mice were obtained by a similar protocol with a 10–100% continuous gradient of OptiPrep (Nycomed, Norway) to improve the yield. Photoreceptor OS membranes isolated from *Wt* and $Nrl^{-/-}$ mice were covalently labeled with fluorescein isothiocyanate (FITC; Invitrogen) by using established protocols (52). FITC-labeled photoreceptor OS membranes were resuspended in DMEM plus streptomycin/penicillin, 10% fetal bovine serum, and 2.5% sucrose; 50 μl of this mixture was added to the top of the transwell membrane, while 700 μl of DMEM alone plus streptomycin/penicillin and 10% fetal bovine serum was added to the well of the plate. Assay mixtures were incubated in the dark at 37°C for 1 h. Cells were washed 3 times with PBS plus 1 mM $MgCl_2$ and 0.2 mM $CaCl_2$ (PBS-MC). FITC fluorescence of externally bound photoreceptor OS was quenched by incubation with 0.2% trypan blue (Invitrogen) for 10 min, after which cells were washed 3 times with PBS-MC. Cells were fixed with ice-cold methanol for 5 min at 4°C followed by 3% paraformaldehyde at room temperature for 10 min. Cells were washed 2 times with PBS-MC and permeablized with 0.2% Triton X-100 in PBS for 30 min at room temperature. Nuclear staining was performed by incubation with Hoechst stain (10 μm final) for 30 min at room temperature. Cells were washed in PBS-MC an additional 3 times. Transwell membranes were removed from supports and mounted onto microscope slides with ProLong Gold Antifade Agent (Invitrogen).

RESULTS

Key features of human ESCS: relationship to the $Nrl^{-/-}$ mouse model

The diagnosis of ESCS is based on a quantitative comparison of S-cone and L/M-cone visual and/or retinal parameters (6, 7, 53, 54). Normally, L/M-cone vision is far more sensitive than S-cone vision, but in ESCS, surprisingly, it is just the opposite. ESCS manifests heightened sensitivity of S-cone vision relative to L/M-cone vision in the presence of little or no rod function. Comparison between a 13-yr-old boy with ESCS [patient 1 (P1)] and a healthy control subject exemplifies the increased S-cone function and reduced L/M-cone vision compared with results in a healthy subject (**Fig. 1*A***). The sensitivity difference is positive

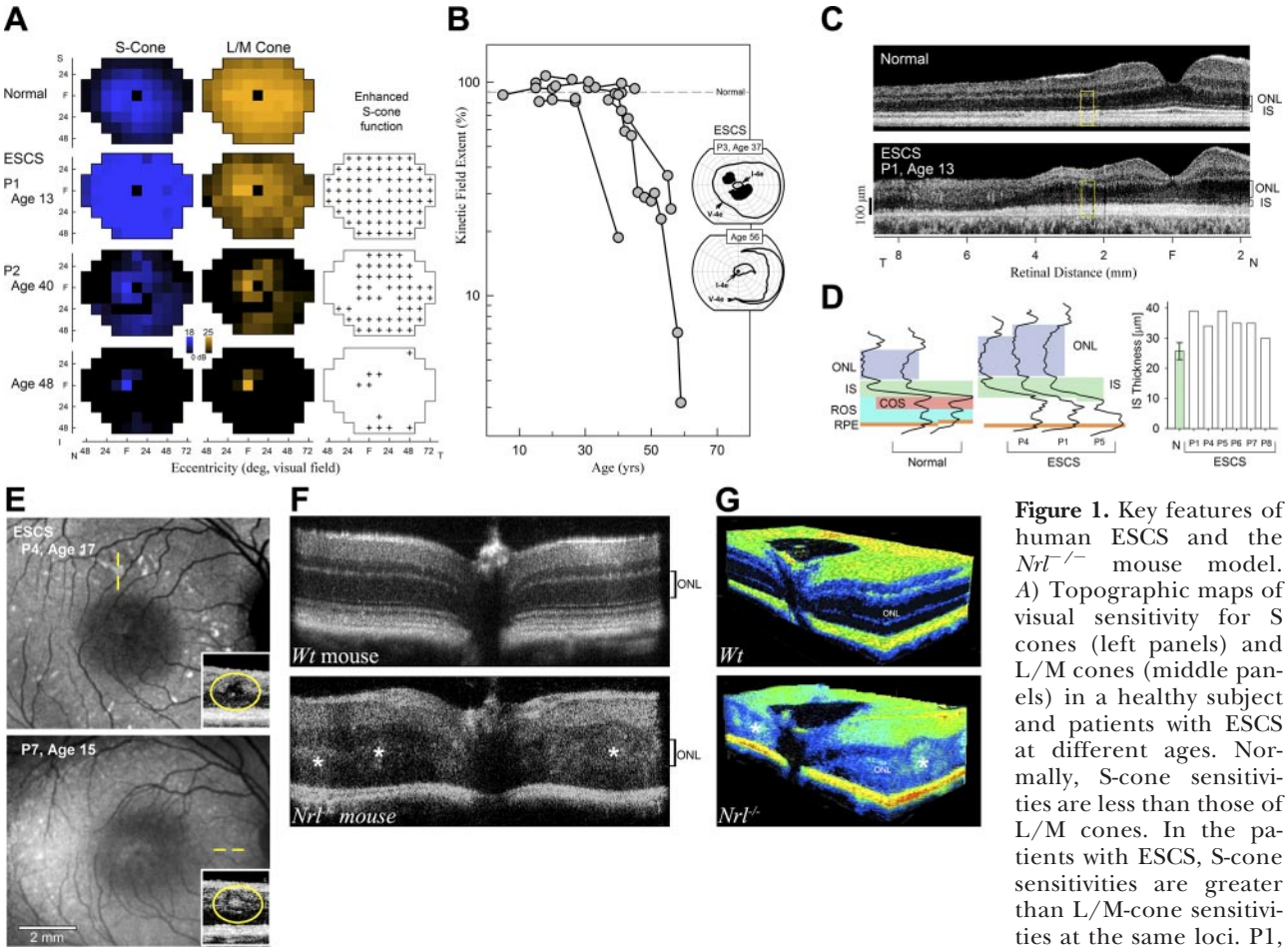

Figure 1. Key features of human ESCS and the $Nrl^{-/-}$ mouse model. *A*) Topographic maps of visual sensitivity for S cones (left panels) and L/M cones (middle panels) in a healthy subject and patients with ESCS at different ages. Normally, S-cone sensitivities are less than those of L/M cones. In the patients with ESCS, S-cone sensitivities are greater than L/M-cone sensitivities at the same loci. P1, a 13-yr-old patient, has supernormal S-cone sensitivities; in P2, at 2 ages (40 and 48 yr), S-cone sensitivities are normal or subnormal but still greater than those of colocalized L/M cones; in the 8-yr interval, a progressive loss of vision was found. Loci showing this positive (enhanced) difference are marked (+, right panels). *B*) Kinetic visual field extent for a large bright target (V-4e) as a function of age in 9 patients with ESCS with longitudinal measurements spanning at least a decade. A decline with age seen in a proportion of these patients is attributable to progressive retinal degeneration. Inset: kinetic fields at 2 ages in ESCS P3 illustrates loss of field extent over a 19-yr interval. *C*) Cross-sectional OCT scans of retinal architecture along >10 mm of the horizontal meridian through the fovea (F) of ESCS P1 (top panel) compared with a healthy subject (top panel). Outer nuclear layer (ONL) and inner segment (IS) thicknesses are labeled at right. Rectangles show temporal retinal region quantified in next panel. *D*) Longitudinal reflectivity profiles (LRPs) of outer retinal lamina in 2 representative healthy subjects (left panel) and 3 patients with ESCS (middle panel). Identifiable layers are labeled and colored. Among notable LRP features are thicker ONL and IS layers in these patients and abnormal structures between the IS and RPE. Quantification of IS thickness in 6 patients with patients with ESCS *vs.* control subjects (right panel) showed a significant difference. *E*) *En face* autofluorescence images of the central fundus of 2 patients with ESCS illustrating hyperautofluorescent features (white dots). Insets: cross-sectional images in colocalized regions show dysmorphology with intraretinal hyperreflective lesions. *F*) OCT of *Wt* and $Nrl^{-/-}$ mouse retinas illustrates phenotypic changes in the $Nrl^{-/-}$ retina resembling those in human ESCS disease; *e.g.*, a hyperreflective RPE-photoreceptor interface and nuclear layer rosette formation (asterisk). ONL thicknesses are labeled at right. *G*) Three-dimensional spectral domain OCT of *Wt* and $Nrl^{-/-}$ mice indicates retinal disorganization caused by rosette formation as well as an abnormal photoreceptor-RPE interaction in the $Nrl^{-/-}$ retina.

(Fig. 1*A*, right panels, denoted by + symbols at test loci) in contrast to negative numbers when normal L/M-cone sensitivities are subtracted from S cones (7). P2, another patient at 2 different ages (40 and 48 yr), shows the same diagnostic difference at loci with persistent function despite reduced S- and L/M-cone vision because of progressive retinal degeneration (Fig. 1*A*). Progressive degenerative retinopathy of ESCS is further illustrated by plotted kinetic visual field data from 9 patients followed longitudinally for at least a decade (Fig. 1*B*). Relatively full visual fields tend to become reduced with age, leaving only central and peripheral islands separated by blind spots (Fig. 1*B*, insets).

In vivo histopathology in early stages of ESCS shows a hyperthick photoreceptor outer nuclear layer (ONL) in the more central retina but a variably reduced ONL with increasing retinal eccentricity (Fig. 1*C*). In the extracentral retina of patients with ESCS, there can be noticeable dysmorphology of the ONL, with intraretinal hyperreflective lesions extending to the inner retina (for example, in P1). Longitudinal reflectivity pro-

files of the outer retinal laminar architecture in 2 healthy subjects at 2.5 mm from the fovea show layers of ONL, photoreceptor inner segments (ISs), rod OSs, cone OSs and RPE (Fig. 1*D*). Three patients with ESCS (ages 17, 13, 31; Fig. 1*D*, middle panel, left to right) definitely have a thickened ONL (55) and appear to have a thickened IS layer as well. When the normal IS layer thickness (n=6, ages 8–29; mean±2SD, 27±2.8 μm) is compared with IS thickness in 6 patients with ESCS (ages 13–31; mean±2SD, 35±6.7 μm), the IS layer in ESCS is significantly thicker (t test, $P<0.001$). This finding may relate to the longer IS in human S cones seen in morphological studies (56). The interface between photoreceptor OS and RPE is also abnormal and ill-defined; *i.e.*, the normal stereotypical multipeaked profile is not evident in patients with ESCS (Fig. 1*D*). The reason for the abnormal interface between photoreceptors and RPE found in these imaging studies is not known. *En face* imaging further illustrated abnormalities in patients with ESCS. In normal subjects, autofluorescence (AF) emissions on short-wavelength excitation are dominated by spatially homogeneous lipofuscin granules accumulated in the RPE (42, 57), but patients with ESCS exhibit hyperautofluorescent loci in the macular and midperipheral retinal regions. Cross-sectional imaging of colocalized regions shows dysmorphology of the ONL extending to the inner retina (Fig. 1*E*, insets; dysmorphology is also seen in the temporal retina of P1, Fig. 1*C*). Abnormal deposition of retinal or RPE fluorophores, unmasking of natural fluorophores by localized loss of RPE melanin, or lipofuscin-laden macrophages, alone or in concert, could contribute to these hyperautofluorescent features (58–60).

The $Nrl^{-/-}$ mice exhibit many phenotypic features of human ESCS disease and thus provide a model to study ESCS pathophysiology. Retinal degeneration is not yet evident at 4 wk of age in the $Nrl^{-/-}$ murine eye. However, cross-sectional optical imaging by SD-OCT revealed abnormal retinal lamination in the $Nrl^{-/-}$ retina compared with *Wt* retina (Fig. 1*F*). Three-dimensional reconstructions allowed visualization of abnormal intraretinal hyperreflective lesions, presumed to be rosettes, and how this distortion affected the retinal laminar architecture (Fig. 1*G*). Plastic block and cryosectioning of retinas further highlighted the dynamic changes resulting from the excessive S-cone photoreceptor population at higher resolution. Compared with normal *Wt* retina (Supplemental Fig. S1*A–D*), the $Nrl^{-/-}$ retina displayed aberrant photoreceptor packing and abnormal association with the RPE (Supplemental Fig. S1*E–H*).

Although these data demonstrate comparable retinal degeneration in human and mouse models of ESCS, the fundamental cellular aberrations that cause this pathophysiology are unknown. We initially approached the molecular basis of this degeneration with a comprehensive global sequencing approach.

Transcriptome analysis by RNA-Seq of retinas from *Wt* and $Nrl^{-/-}$ mice

By sequencing mature *Wt* and $Nrl^{-/-}$ ocular tissues, we determined global changes resulting from knockout of the *Nrl* transcription factor. The reproducibility of RNA-Seq for murine eye was verified by carrying out technical replicates of *Wt* eye samples (R^2=0.98; Supplemental Fig. S2*A*), indicating a minimal variability from run to run. This reproducibility indicated that any differences between tissue samples were not inherent to instrument read errors. *Wt* retinal tissue (**Fig. 2*A***) generated 11,677 unique transcripts at a level of 1 FPKM or higher (Fig. 2*B*) whereas $Nrl^{-/-}$ retinal tissue (Fig. 2*C*) generated 11,778 unique transcripts at a level of 1 FPKM or higher (Fig. 2*D*). As expected, in *Wt* and $Nrl^{-/-}$ retinal tissues, a large proportion of transcripts had no annotated function. A complete categorization of Gene Ontology (GO) terms from these tissues is shown in **Table 1**. RNA-Seq expression analysis on whole-eye tissues of *Wt* and $Nrl^{-/-}$mice is summarized in Supplemental Fig. S2*C–F*. The RNA-Seq findings revealed that, across experiments, the number of transcripts detected between runs was not drastically different, nor was their categorization, indicating there is not a gross difference between *Wt* and $Nrl^{-/-}$ retinas and eyes, but rather more subtle differences that require RNA-Seq single-gene resolution to tease out their precise differential expression patterns.

Verification of sequencing data by RT-PCR

Differential expression of transcripts was analyzed by comparing FPKM values between *Wt* and $Nrl^{-/-}$retinal (Fig. 2*E*) and whole-eye (Supplemental Fig. S2*B*) tissues. Previous microarray studies have used an empirical cutoff of a 1.5-fold average change as the minimum to identify a difference between the *Wt* and $Nrl^{-/-}$ genotypes (26). Using this same cutoff, we identified 7316 and 6203 differentially expressed transcripts in whole-eye and retinal samples, respectively. Previous studies have used *in situ* hybridization and RT-PCR to verify results of microarray analyses (26, 28), results of which overlapped with our current RNA-Seq data (Fig. 2).Therefore, we chose to use RT-PCR to verify differentially expressed transcripts identified by RNA-Seq. Compared with the 66 transcripts that were differentially expressed and overlapped with findings of all 3 studies, RT-PCR had been done previously with 31 of these targets (26), and our RNA-Seq data indicated an excellent correlation of fold differences between *Wt* and $Nrl^{-/-}$ retinal tissues for these 31 targets (R^2=0.91). We also performed RT-PCR on targets representing a new signaling pathway that may dictate the formation and maintenance of the cone-line environment in the $Nrl^{-/-}$ retina. We chose transcripts with large differential expression (*Egr1, Opn1sw*), more subtle changes (*Gdf11, Otx2, Thrb*) and no significant change (*Crx*). The results of our RT-PCR strongly correlated with the differential expression detected by

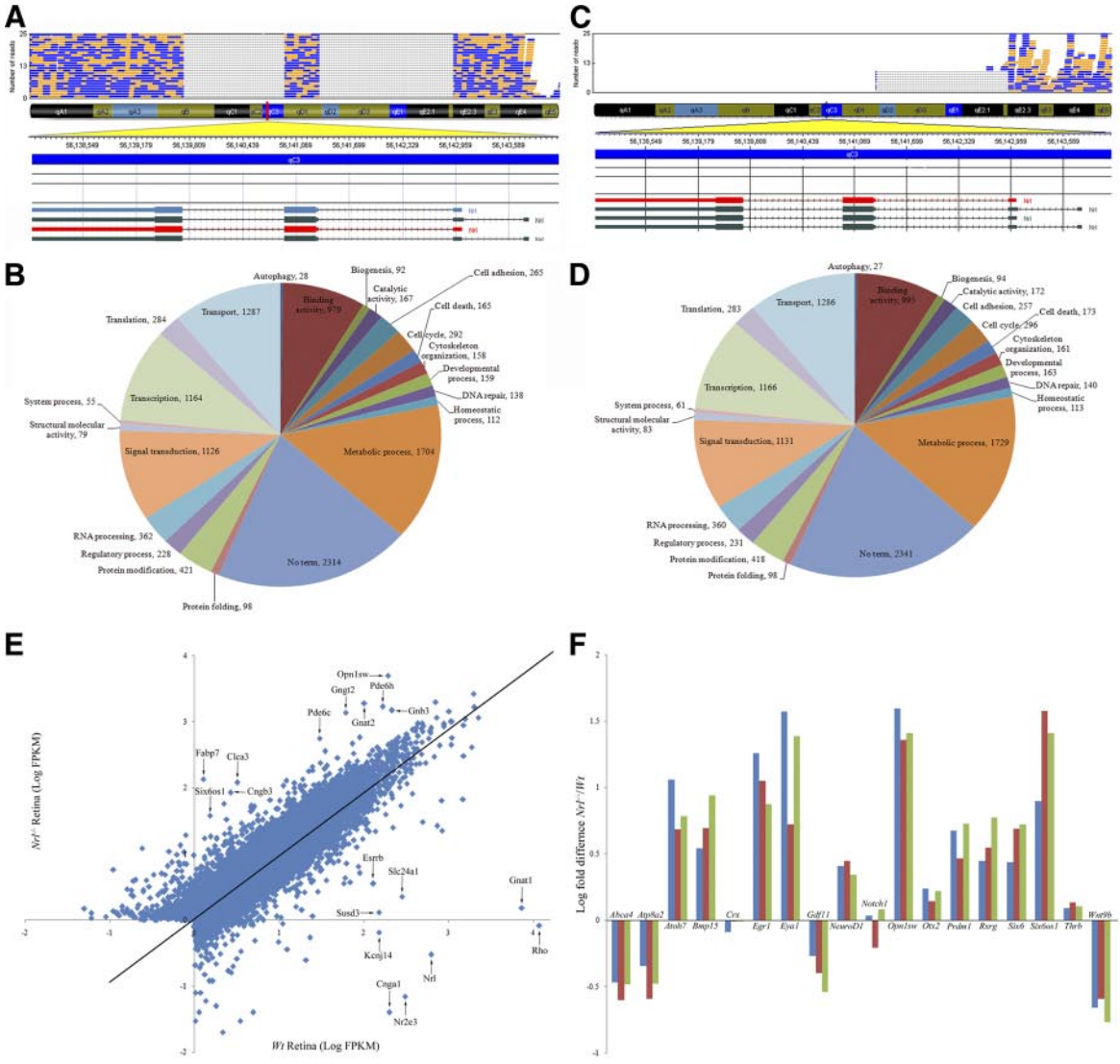

Upregulated	1.5-2 fold	2-3 fold	3-5 fold	>5 fold
Microarray Studies	16	49	48	75
RNA-Seq Study	1381	713	165	91

Downregulated	1.5-2 fold	2-3 fold	3-5 fold	>5 fold
Microarray Studies	20	56	94	175
RNA-Seq Study	1916	1402	378	157

TABLE 1. *GO term breakdown of transcript reads across different RNA-Seq experiments with* Wt *and* $Nrl^{-/-}$ *tissues*

	Retina		Eye	
GO term	*Wt*	$Nrl^{-/-}$	*Wt*	$Nrl^{-/-}$
Autophagy	28 (0.24)	27 (0.23)	28 (0.21)	28 (0.21)
Binding activity	979 (8.38)	995 (8.45)	1186 (8.85)	1190 (8.90)
Biogenesis	92 (0.79)	94 (0.80)	102 (0.76)	103 (0.77)
Catalytic activity	167 (1.43)	172 (1.46)	189 (1.41)	192 (1.44)
Cell adhesion	265 (2.27)	257 (2.18)	330 (2.46)	329 (2.46)
Cell cycle	292 (2.50)	296 (2.51)	353 (2.63)	349 (2.61)
Cell death	165 (1.41)	173 (1.47)	203 (1.51)	202 (1.51)
Cytoskeleton organization	158 (1.35)	161 (1.37)	183 (1.37)	181 (1.35)
Developmental process	159 (1.36)	163 (1.38)	203 (1.51)	201 (1.50)
DNA repair	138 (1.18)	140 (1.19)	159 (1.19)	157 (1.17)
Homeostatic process	112 (0.96)	113 (0.96)	123 (0.92)	122 (0.91)
Metabolic process	1704 (14.59)	1729 (14.68)	1983 (14.79)	1979 (14.78)
No term	2314 (19.82)	2341 (19.88)	2570 (19.17)	2599 (19.44)
Protein folding	98 (0.84)	98 (0.83)	101 (0.75)	102 (0.76)
Protein modification	421 (3.61)	418 (3.55)	508 (3.79)	500 (3.74)
Regulatory process	228 (1.95)	231 (1.96)	271 (2.02)	271 (2.03)
RNA processing	362 (3.10)	360 (3.06)	392 (2.92)	391 (2.92)
Signal transduction	1126 (9.64)	1131 (9.60)	1354 (10.10)	1337 (10.00)
Structural molecule activity	79 (0.68)	83 (0.70)	107 (0.80)	107 (0.80)
System process	55 (0.47)	61 (0.52)	86 (0.64)	91 (0.68)
Transcription	1164 (9.97)	1166 (9.90)	1255 (9.36)	1250 (9.35)
Translation	284 (2.43)	283 (2.40)	286 (2.13)	286 (2.14)
Transport	1287 (11.02)	1286 (10.92)	1434 (10.70)	1404 (10.50)
Total transcripts (≥1 FPKM)	11677	11778	13406	13368

All transcripts detected at a level of 1 FPKM in *Wt* and $Nrl^{-/-}$ tissue samples were categorized by GO term categorization using AmiGO 1.8. Values represent number of transcripts, with percentage of total transcripts in parentheses. We had fewer total transcripts in the retina sample runs compared to the eye, since we examined a more specialized tissue of the whole. The number of transcripts in each category did not greatly vary between *Wt* and $Nrl^{-/-}$ samples. This finding indicated that the knockout of *Nrl* causes relatively subtle differences in the overall gene network to mimic the human ESCS phenotype.

RNA-Seq analyses of the retina and whole eye (Fig. 2*F*). Given the precise quantification of the transcript levels, we calculated that the signal needed for detecting a fold change of 1.5 with statistical significance required only 2 biological samples. In addition, because this trend in differential expression was preserved in RNA-Seq runs of the whole eye and retina (**Table 2**), this also indicates that the detected unique transcripts truly represent significant changes between the *Wt* and $Nrl^{-/-}$ genotypes. Therefore, a

Figure 2. RNA-Seq of *Wt* and $Nrl^{-/-}$ retinas reveals new differentially expressed genes arising from transcriptional misregulation. *A*) *Wt* retina RNA-Seq run, represented by robust *Nrl* transcript detection, detected 11,677 transcripts at 1 FPKM or higher. *B*) Pie chart shows breakdown of GO term categories to which the transcripts are assigned, with the number of transcripts in each category indicated. *C*) Single-base resolution of the RNA-Seq run of $Nrl^{-/-}$ retina reveals ablation of *Nrl* transcript detection in the regions of exon 2 and 3 where there is a neomycin cassette. *D*) Run detected 11,778 transcripts at 1 FPKM or higher; pie chart shows breakdown of GO term categories to which the transcripts are assigned, with the number of transcripts in each category indicated. *E*) RNA-Seq runs of *Wt* and $Nrl^{-/-}$ retina are plotted to show their differential expression pattern. Plots of Log FPKM of the retinal runs of *Wt* and $Nrl^{-/-}$ illustrate that, whereas the majority of reads fall along the line representing equal expression, a range of transcripts falls either above or below the line that represent differentially expressed transcripts. *Cnga1*, *Esrrb*, *Gnat1*, *Kcnj14*, *Nr2e3*, *Nrl*, *Rho*, *Slc24a1*, and *Susd3* (arrows) are among the highest expressed transcripts in the *Wt* retina, whereas *Clca3*, *Cngb3*, *Fabp7*, *Gnat2*, *Gnb3*, *Gngt2*, *Opn1sw*, *Pde6c*, *Pde6h*, and *Six6os1* (arrows) are among the highest expressed transcripts in the $Nrl^{-/-}$ retina RNA-Seq run. *F*) RT-PCR validated differential expression patterns detected by RNA-Seq. To validate differences from RNA-Seq experiments, retinal tissue from *Wt* and $Nrl^{-/-}$ mice was used for RT-PCR using probes against well characterized targets from previous studies as well as newly identified targets from the current RNA-Seq study. RT-PCR results validated the RNA-Seq differential expression pattern that ranged from those genes that were highly differentially expressed (*Egr1*, *Opn1sw*) to those with more subtle differential expression (*Gdf11*, *Otx2*, *Thrb*) and even those without a significant fold change (*Crx*). Blue bars indicate RT-PCR of retina; red bars, RNA-Seq of whole eye; green bars, RNA-Seq of retina. Current RNA-Seq experiment, when compared to 2 previous microarray studies looking at differential expression between *Wt* and $Nrl^{-/-}$ retina, reveals more comprehensive and quantitative data. *G*) RNA-Seq data reveal 3659 unique transcripts up-regulated in the $Nrl^{-/-}$retina compared to previous data sets, indicating a considerable amount of newly differentially expressed transcripts compared to previous findings. Moreover, the bottom panel shows that whereas microarray studies can assess gross changes well (5-fold or greater), more subtle changes in differential expression are more robustly characterized using RNA-Seq. *H*) RNA-Seq reveals 2230 unique transcripts down-regulated in the $Nrl^{-/-}$retina compared to previous data sets. The bottom panel again highlights the greater coverage of differential expression at lower thresholds using RNA-Seq.

TABLE 2. *Fold changes of selected transcripts in* Nrl$^{-/-}$ *relative to* Wt *tissue across different experiments*

Gene	RT-PCR	Retina RNA-Seq	Eye RNA-Seq
Abca4	−2.94	−3.05	−3.98
Atp8a2	−2.22	−3.02	−3.90
Atoh7	11.44	6.07	4.83
Bmp15	3.48	8.75	4.96
Crx	−1.22	−1.02	−1.02
Egr1	18.26	7.46	11.20
Eya1	37.48	24.35	5.26
Gdf11	−1.85	−3.45	−2.50
Neurod1	2.57	2.20	2.80
Notch1	1.08	1.21	0.62
Opn1sw	39.32	25.89	22.93
Otx2	1.73	1.66	1.39
Prdm1	4.74	5.33	2.93
Rxrg	2.81	5.96	3.52
Six6	2.75	5.26	4.87
Six6os1	7.89	25.83	37.91
Thrb	1.24	1.27	1.37
Wnt9b	−4.55	−5.88	−3.92

Fold change of selected transcripts was well preserved across different experiments. Targets chosen for validation included genes whose expression changed greatly (*Opn1sw*, *Eya1*, *Egr1*), genes with more subtle fold changes (*Gdf11*, *Otx2*, *Thrb*) and *Crx*, which had no significant change. Fold changes determined by RNA-Seq correlated well with changes in tissue expression of transcripts in both eye and retina.

thorough analysis of the murine retina transcriptome was well warranted.

Characterizing differentially expressed transcripts

Direct comparison of previous retinal microarray studies (26, 28) with the RNA-Seq of the *Wt* and *Nrl*$^{-/-}$ retina revealed that of the 6203 differentially expressed transcripts, 5889 were unique to this study, with 3659 of the transcripts up-regulated (Fig. 2*G*) and 2230 transcripts down-regulated (Fig. 2*H*) in the *Nrl*$^{-/-}$retina. The greater number of up-regulated as compared to down-regulated transcripts using the same thresholds is similar to what was reported in previous microarray experiments (28). Breakdown of transcripts by their fold change revealed that RNA-Seq identified more subtle changes in transcript levels than microarrays (Fig. 2*G*, *H*).

Examination of transcripts with large differences between *Wt* and *Nrl*$^{-/-}$ expression revealed 248 transcripts to differ by 5-fold or more, of which 134 were unique to this study. Pathway analysis was done for all 248 transcripts. In particular, analysis of the 134 unique transcripts identified several that were critical in pathways involved in photoreceptor differentiation and maintenance, such as atonal homologue 7 (*Atoh7/Math5*), a bHLH factor involved in Notch signaling (61); *Six6*, a sine oculis-related homeobox gene in the pathway of the master regulatory genes of eye development, *Pax6* and *Eya1* (62–68); and desert hedgehog (*Dhh*), a sonic hedgehog signaling molecule (69, 70). Furthermore, several key developmental maintenance pathways, such as the Wnt (71, 72) and Bmp signaling pathways (73, 74) had misexpressed transcripts in the *Nrl*$^{-/-}$ retina, such as *Wnt9b* and *Bmp15*. Pathway analyses of these transcripts, coupled with other transcripts found in this and previous studies to be misregulated, provide a more comprehensive transcriptional landscape to examine S-cone commitment and maintenance in the *Nrl*$^{-/-}$ mouse retina. Notably, 29 of 134 transcripts have no annotated function and thus represent new targets for study of cone-like photoreceptor maintenance and function.

Examination of homeostatic processes involved in photoreceptor function in the visual cycle revealed cone signature genes (*Pde6c* and *Cngb3*, among others). It also revealed down-regulated genes important for retinoid metabolism and clearance of potentially toxic photooxidized compounds (*Abca4*, *Rdh12*, and *Rdh5*, among others; **Table 3**). In contrast, expression of genes encoding putative proteins involved in RPE-mediated phagocytosis responsible for toxic metabolite removal and recycling were unchanged. However, key photoreceptor ligands necessary for phagocytosis, *Tub* and *Tulp1* (75), were down-regulated in the *Nrl*$^{-/-}$ retina (**Table 4**). Down-regulation of key retinoid metabolic genes, coupled with down-regulation of *Tub* and *Tulp1*, suggested a potential mechanism involving defective phagocytosis underlies the photoreceptor degeneration seen in ESCS. Therefore, to verify a potential aberrant phagocytotic process, we sought to verify the differential expression changes identified by RNA-Seq by complementary methods, including high-resolution imaging studies.

Disrupted ESCS retinal architecture and patchy loss of photoreceptors

Overproduction of short-wavelength-sensitive photoreceptors in patients with ESCS causes retinal disorganization and has been analyzed only by conventional optical methods. The *Nrl*$^{-/-}$ mouse retina offers the possibility to investigate the structural phenotype in greater detail. Confocal microscopy imaging of *Nrl*$^{-/-}$ mouse retinal whole mounts dramatically illustrated disrupted architecture in 3-D space (**Fig. 3**). When compared to cone-like photoreceptor packing in *Wt* mouse retina (Fig. 3*A*, *B*), *Nrl*$^{-/-}$ retina exhibited aberrant clustering of photoreceptors with empty patches where nuclear rosettes had formed (Fig. 3*G*, *H*). *Wt* retinal whole mounts stained for both rods and cones displayed the entire area populated by photoreceptors (Fig. 3*C*, *D*), whereas *Nrl*$^{-/-}$ retinal mounts featured irregular photoreceptor packing (Fig. 3*G*, *H*). Notably, *Nrl*$^{-/-}$ photoreceptor density was clearly reduced, as indicated by empty patches of retina that lacked photoreceptor staining (Fig. 3*I*, *J*).

To probe the photoreceptor morphology, we prepared critical point dried retinas separated from the RPE of both *Wt* and *Nrl*$^{-/-}$ 4-wk-old mice. As noted from previous work (51), SEM imaging revealed that

TABLE 3. *Transcript levels of visual cycle proteins in* Nrl$^{-/-}$ *relative to* Wt *tissue across different RNA-Seq runs*

	Retina RNA-Seq			Eye RNA-Seq		
Gene	*Wt*	*Nrl*$^{-/-}$	Fold difference[a]	*Wt*	*Nrl*$^{-/-}$	Fold difference[a]
Abca4	175.71	57.62	0.33	90.25	22.51	0.25
Arr3	88.55	578.24	6.53	62.25	302	4.85
Cnga1	198.7	0.04	—	148.55	0	—
Cnga3	4.63	44.45	9.60	2.18	21.64	9.93
Cngb3	2.66	84.83	31.89	1.34	42.98	32.07
Gnat1	7281.64	1.53	—	4311.21	1.02	—
Gnat2	100.61	1924.72	19.13	67.4	951.07	14.11
Gnb1	1472.44	67.23	0.05	1400.74	121.52	0.09
Gnb2	76.18	88.58	1.16	124.9	92.93	0.74
Gnb3	214.35	1481.55	6.91	144.04	815.01	5.66
Gngt1	304.41	574.91	1.89	209.38	591.24	2.82
Gngt2	60.66	1379.01	22.73	91.18	1465.48	16.07
Guca1a	720.15	1150.14	1.60	749.33	553.63	0.74
Guca1b	827.36	64.27	0.08	625.54	25.57	0.04
Gucy1a3	33.47	39.42	1.18	19.16	25.01	1.31
Gucy1b3	32.67	39.5	1.21	38.38	56.48	1.47
Gucy2e	114.93	22.17	0.19	48.5	15.56	0.32
Gucy2f	20.73	0.25	0.01	10.82	0.37	0.03
Lrat	2.36	3.5	1.48	14.64	15.01	1.03
Opn1mw	137.65	246.42	1.79	49.12	136.56	2.78
Opn1sw	191.93	4968.88	25.89	120.49	2762.3	22.93
Pde6a	492.09	30.48	0.06	243.91	12.2	0.05
Pde6b	736.22	26.53	0.04	527.87	16.87	0.03
Pde6c	30.13	564.61	18.74	31.17	512.77	16.45
Pde6d	68.19	118.06	1.73	54.08	85.73	1.59
Pde6g	2250.16	1151.56	0.51	1561.58	639.69	0.41
Pde6h	166.22	1700.2	10.23	105.58	959.4	9.09
Ppp2r4	55.13	42.87	0.78	52.08	35.72	0.69
Rbp3	1093.27	1017.07	0.93	440.05	430.68	0.98
Rcvrn	1068.31	446.34	0.42	787.61	295.54	0.38
Rdh12	215.6	70.46	0.33	132.14	44.55	0.34
Rdh5	21.19	23.91	1.13	130.08	69.71	0.54
Rdh8	78.11	33.36	0.43	45.53	13.02	0.29
Rgs9	105.31	53.94	0.51	119.26	81.97	0.69
Rgs9bp	151.7	86.18	0.57	91.56	38.6	0.42
Rho	11745.08	0.83	—	6575.59	0.67	—
Rpe65	9.21	20.42	2.22	52.64	65.66	1.25
Sag	2021.36	1659.71	0.82	1181.97	768.89	0.65

Differential expression pattern in *Nrl*$^{-/-}$ mice compared to *Wt* in transcript levels (FPKM) elucidates those transcripts that are essential for rod and cone function and maintenance. Fold differences, preserved across eye and retina RNA-Seq runs, illustrate noticeable enrichment of *Cnga3*, *Cngb3*, *Gnb3*, *Gngt2*, *Pde6c*, and *Pde6h* in *Nrl*$^{-/-}$ mice, highlighting their role in cone-like photoreceptor function and maintenance. Conversely, the noticeable reduction of *Cnga1*, *Gnat1*, *Gnb1*, *Guca1b*, *Gucy2f*, *Pde6a*, and *Pde6b* in *Nrl*$^{-/-}$ mice points out the importance of these transcripts in rod photoreceptor function and maintenance. In addition, many visual cycle proteins involved in retinoid metabolism, such as Abca4, Rdh12, and Rdh5, have attenuated transcript expression in *Nrl*$^{-/-}$ mice, suggesting a misregulation of this process compared to *Wt* mice.
[a]Fold differences cannot be accurately determined for transcripts that are almost completely absent in *Nrl*$^{-/-}$ mice.

Wt retina contained tightly packed, cylindrically shaped rod photoreceptors (Fig. 3*E*, *F*). In contrast, *Nrl*$^{-/-}$ photoreceptors exhibited a different structure and packing arrangement. In agreement with whole-mount confocal microscopy imaging, SEM imaging showed patches of ESCS photoreceptors clustered together and separated by patches devoid of photoreceptors (Fig. 3*K*). When these photoreceptors were probed at higher magnification, their OS appeared bulbous (Fig. 3*L*). This abnormal phenotype could explain why the packing density of photoreceptors is greatly reduced in ESCS (n=5, 0.38±0.04 photoreceptors/μm^2) relative to *Wt* retina (n=5, 0.86±0.06 photoreceptors/μm^2) when analyzing the SEM data. To better understand the structural defect contributing to this bulbous OS phenotype in *Nrl*$^{-/-}$ photoreceptors, we studied thin sections of photoreceptors by TEM to examine their internal architecture.

ESCS photoreceptors exhibit abnormal accumulations of material

Thin sections of retina were prepared and examined by TEM. *Wt* rods displayed neatly stacked discrete discs (Fig. 3*M*, *N*). Because these blocks were prepared shortly after the onset of light, coinciding with the peak

TABLE 4. *Transcript levels of putative phagocytosis proteins in* Nrl$^{-/-}$ *relative to* Wt *tissue across different RNA-Seq runs*

	Retina RNA-Seq			Eye RNA-Seq		
Gene	*Wt*	*Nrl*$^{-/-}$	Fold difference	*Wt*	*Nrl*$^{-/-}$	Fold difference
Anxa2	12.02	17.64	1.47	491	285.3	0.58
Axl	4.25	4.85	1.14	16.08	13.42	0.83
Cd36	0.45	1.13	2.51	11.18	30.48	2.73
Cd81	131.05	138.36	1.06	121.55	166.18	1.37
Gas6	125.26	78.05	0.62	175.97	95.2	0.54
Itgav	5.99	11.85	1.98	9.53	14.55	1.53
Itgb5	21.75	20.38	0.94	91.7	56.22	0.61
Mertk	1.82	2.44	1.34	3.38	2.97	0.88
Mfge8	190	155.59	0.82	253.06	173.92	0.69
Ptk2 (Fak)	9.37	12.39	1.32	15.04	14.8	0.98
Src	16.61	9.39	0.57	40.92	18.87	0.46
Tub	75.26	30.46	0.40	50.16	17.99	0.36
Tulp1	478.55	325.02	0.68	295.93	180.83	0.61
Tyro3	8.77	1.93	0.22	13.4	4.35	0.32

Differential expression pattern in *Nrl*$^{-/-}$ mice compared to *Wt* in transcript levels (FPKM) elucidates those transcripts that are essential for rod and cone function and maintenance. Fold differences, preserved across eye and retina RNA-Seq runs, illustrate noticeable enrichment of *Cnga3*, *Cngb3*, *Gnb3*, *Gngt2*, *Pde6c*, and *Pde6h* in *Nrl*$^{-/-}$ mice, highlighting their role in cone-like photoreceptor function and maintenance. Conversely, the noticeable reduction of *Cnga1*, *Gnat1*, *Gnb1*, *Guca1b*, *Gucy2f*, *Pde6a*, and *Pde6b* in *Nrl*$^{-/-}$ mice points out the importance of these transcripts in rod photoreceptor function and maintenance. In addition, many visual cycle proteins involved in retinoid metabolism, such as Abca4, Rdh12, and Rdh5 have attenuated transcript expression in *Nrl*$^{-/-}$ mice, suggesting a misregulation of this process compared to *Wt* mice.

of OS disc shedding (3), imaging of the photoreceptor-RPE interface also revealed phagosomes that dispose of shed OS disc membranes (Fig. 3*O*). TEM imaging of photoreceptors in *Nrl*$^{-/-}$ retina showed an OS disc arrangement distinctly different from rods (Fig. 3*P*), with some discs exhibiting interconnections to each other and the surrounding plasma membrane (Fig. 3*P*, *Q*). An abnormal buildup of material in ESCS photoreceptors was found at the photoreceptor-RPE interface (Fig. 3*R*). OS tips of these photoreceptors were enlarged because of an internal buildup of vacuole-like structures. By 8 wk of age, when degeneration is present, thin sections of *Nrl*$^{-/-}$ retina revealed photoreceptor OS that exclusively contained vacuole-like structures with only a few disc elements present (Supplemental Fig. S3*A*, *B*).

Evidence for aberrant phagocytosis in ESCS disease

Phagocytosis is a dynamic process that occurs across the entire retina. Therefore, a hybrid SEM technique, SBF imaging, was used to cover a large area of the retina and capture serial sections of the photoreceptor-RPE interface to identify any abnormalities that might relate to this process. The block face was imaged by backscattered electrons after a 100-nm section was removed by a microtome inside the scanning electron microscope. This process was repeated to allow sectioning and imaging of the entire RPE to visualize the phagocytic process that occurs during OS disc shedding. SBF-SEM imaging revealed that the photoreceptor-RPE interface in the *Wt* sample has an orderly architecture with tightly stacked rods apposed to the interface where shed disc membranes are clearly engulfed (**Fig. 4*A*, *B*** and Supplemental Movie S1). Moreover, 3-D reconstructions revealed that these phagosomes were present throughout the RPE (Fig. 4*C*), demonstrating that this technique can capture a dynamic process occurring across multiple planes of the retina. When *Nrl*$^{-/-}$ mouse retina was subjected to SBF-SEM imaging, the photoreceptors were not tightly packed at the RPE interface, and they also exhibited the abnormal associations with the RPE previously noted. Furthermore, the aberrant diseased OS head phenotype was visible in some sections (Fig. 4*D–E* and Supplemental Movie S1), but no phagosomes were seen throughout the retina, despite sectioning through multiple RPE cells. Given that a proportion of cone photoreceptors is renewed daily (4, 5), it is noteworthy that not a single phagosome was identified, indicating severely reduced RPE phagocytosis of OS in this ESCS model. Three-dimensional reconstructions further illustrated the lack of phagosomes in the RPE and confirmed the presence of abnormal photoreceptor OS heads at the RPE interface (Fig. 4*F*).

The compromised phagocytic process identified in *Nrl*$^{-/-}$ mice was subsequently confirmed by staining for phagosomes at the RPE-photoreceptor interface. Cryosectioned retinas were stained with an antibody against PS, the most abundant anionic phospholipid (76) and a key component of phagosomes (77, 78), asymmetrically situated in the inner leaflet of their plasma membranes (79). Because PS is present in most cell membranes (80), low detergent concentrations (0.3% Triton) were used to selectively detect PS staining of shed disc membranes. In *Wt* mouse retina, PS staining identified phagosomes at the photoreceptor-RPE interface (**Fig. 5**). PS staining colocalized with shed discs labeled for cone opsin, confirming that staining at the

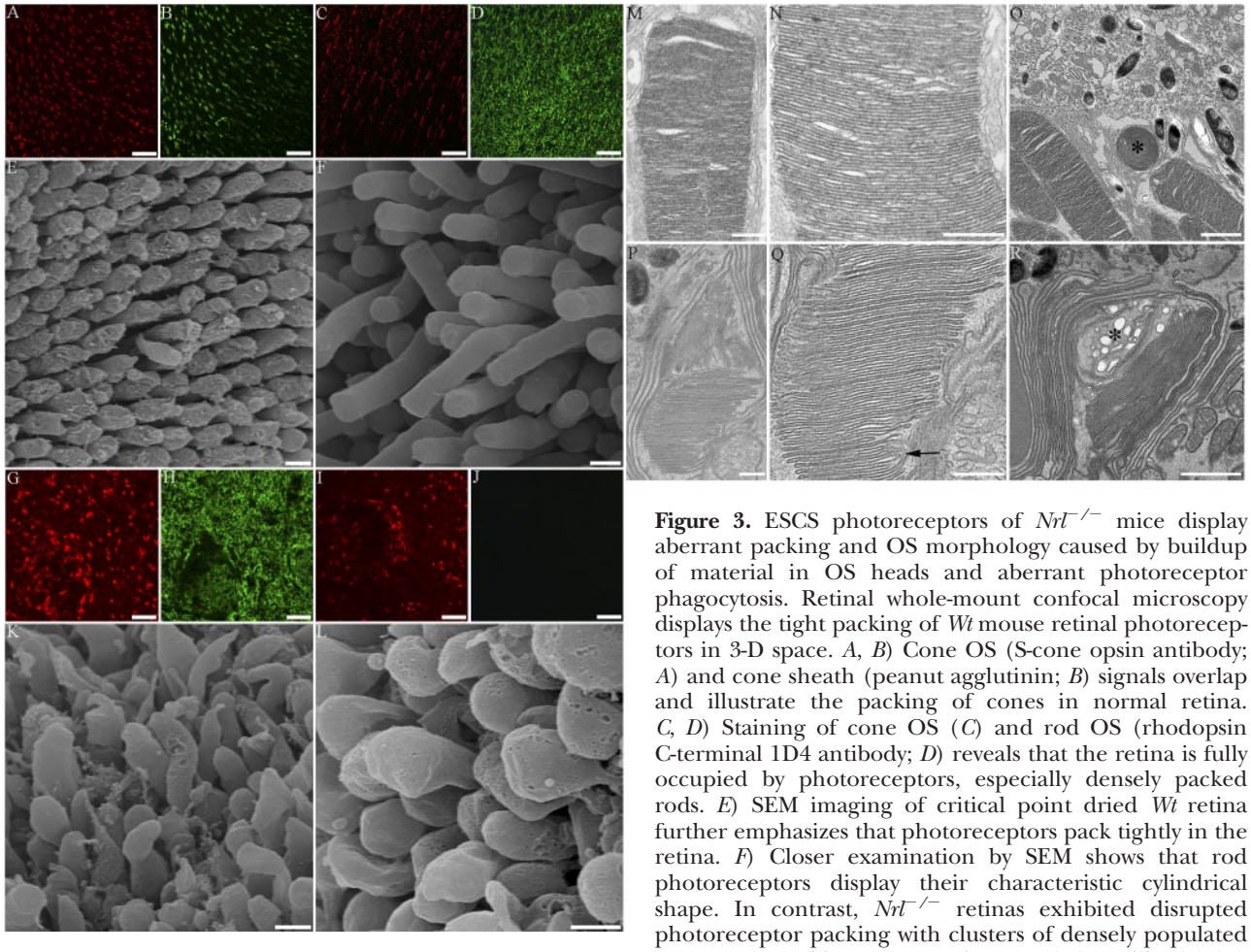

Figure 3. ESCS photoreceptors of $Nrl^{-/-}$ mice display aberrant packing and OS morphology caused by buildup of material in OS heads and aberrant photoreceptor phagocytosis. Retinal whole-mount confocal microscopy displays the tight packing of *Wt* mouse retinal photoreceptors in 3-D space. *A*, *B*) Cone OS (S-cone opsin antibody; *A*) and cone sheath (peanut agglutinin; *B*) signals overlap and illustrate the packing of cones in normal retina. *C*, *D*) Staining of cone OS (*C*) and rod OS (rhodopsin C-terminal 1D4 antibody; *D*) reveals that the retina is fully occupied by photoreceptors, especially densely packed rods. *E*) SEM imaging of critical point dried *Wt* retina further emphasizes that photoreceptors pack tightly in the retina. *F*) Closer examination by SEM shows that rod photoreceptors display their characteristic cylindrical shape. In contrast, $Nrl^{-/-}$ retinas exhibited disrupted photoreceptor packing with clusters of densely populated cones separated by empty patches. *G*, *H*) Cone-like OS (*G*) and extracellular sheath (*H*) signals overlap but also are absent from some retinal patches. *I*, *J*) Staining of cone OS (*I*) and rod OS (*J*) reveals only ESCS photoreceptors. *K*) SEM imaging of critical point dried $Nrl^{-/-}$ retina shows disrupted packing of photoreceptors in the retina, with a less dense population of photoreceptors than *Wt*. *L*) Closer examination by SEM highlights abnormal OS morphology with enlarged head structures. *M–R*) Thin-sectioned retinas from *Wt* and $Nrl^{-/-}$ mice were prepared for TEM imaging. *M*) Thin sectioning of *Wt* retina reveals the internal structure of photoreceptors. *N*) Discrete stacked discs are seen in rod photoreceptors. *O*) Because these samples were prepared at the peak of photoreceptor turnover, TEM imaging captures the disc shedding process and RPE mediated phagocytosis (asterisk). *P*) Thin sectioning of $Nrl^{-/-}$ retina shows a distinctive OS disc arrangement that differs from *Wt* rods. *Q*) Discs retain some interconnections (arrow) as well as connections to the plasma membrane. *R*) Closer examination of ESCS photoreceptors reveals that most photoreceptors have enlarged head structures owing to buildup of material at the photoreceptor-RPE interface (asterisk), which would not occur with normal phagocytosis. Scale bars = 5 μm (*A–D*, *G–J*); 1 μm (*E*, *F*, *K*, *L*, *O*, *R*); 250 nm (*M*, *N*, *P*, *Q*).

photoreceptor-RPE interface truly captured shed disc phagosomes (Fig. 5*A*, *D*). Light and confocal microscopy of cryosectioned retinas and stained eye whole mounts also revealed that this phagosome staining was located at the RPE-photoreceptor plane interface (Fig. 5*E*, *F*). When the same experiments were performed with $Nrl^{-/-}$ mice, no such staining was found at the photoreceptor-RPE interface, either in cryosectioned retinas (Fig. 5*G*) or eye whole mounts (Fig. 5*H*). Similar experiments were done with an anti-annexin V antibody, which also recognizes PS, albeit less specifically (81), with results consistent with those obtained with the anti-PS antibody. Because phagocytosis depends on both proper signaling from shed disc packets and recognition of this signal by the neighboring RPE, we finally sought to understand whether the $Nrl^{-/-}$ phagocytotic defect was due to an inherent abnormality of the photoreceptors or the RPE.

ESCS phenotype attributed to photoreceptor abnormalities rather than an RPE defect

The RPE plays a critical role in retinal maintenance. Thus, the defect in $Nrl^{-/-}$ mice and humans with ESCS may be attributable not only to aberrant photoreceptors that result in this disease but also to defective RPE cells that interface with these photoreceptors. To investigate these possibilities, we cultured isolated RPE cells from *Wt* and $Nrl^{-/-}$ eyes (50). The yield from both types of mice was comparable. Purified OS membrane vesicles from *Wt* and $Nrl^{-/-}$ animals then were used to

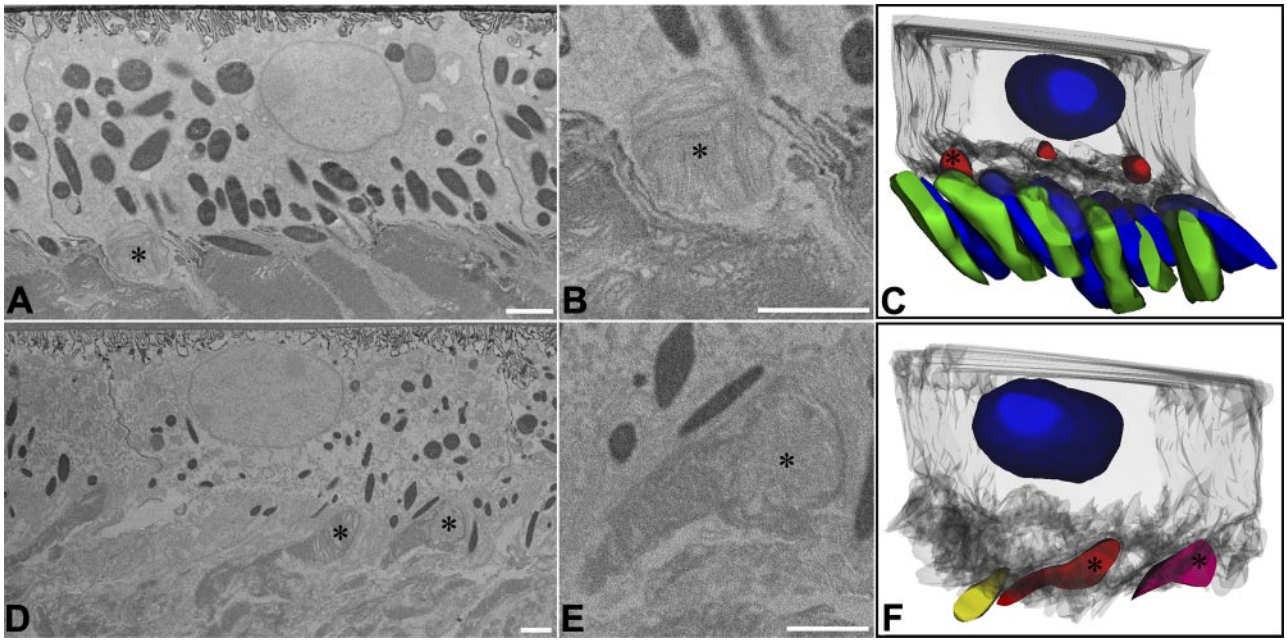

Figure 4. SBF-SEM allows visualization of impaired phagocytosis present in ESCS retinal degeneration. Because photoreceptor disc phagocytosis is a dynamic process that occurs throughout the retina, SBF-SEM imaging was used to collect precise serial sections and investigate phagocytosis of shed discs. *A*) In *Wt* retina, the photoreceptor-RPE interface is clearly visible, with tight packing of rods opposed to the RPE (see Supplemental Movie S1). *B*) Moreover, phagosomes (asterisk) ingested by the RPE are clearly visible. *C*) Three-dimensional reconstructions of collected data with Reconstruct allow visualization of multiple phagosomes (red), including the one indicated by asterisk in panels *A, B*, throughout a RPE cell (gray, with nucleus in blue) and also reveal the tight packing of rods (green and blue) in a plane. *D*) In $Nrl^{-/-}$ retina, the photoreceptor-RPE interface is visible, but photoreceptors (asterisks) are not as densely packed against the RPE (see Supplemental Movie S1). *E*) Enlarged OS head structures of ESCS photoreceptors (asterisk) are seen with less electron-dense material at the tips, indicating loss of OS material in that area. *F*) Resulting 3-D reconstruction illustrates these enlarged headed photoreceptors (asterisks) and their interactions with the RPE (gray, with nucleus in blue). Of note is the absence of any visible phagosomes within the modeled $Nrl^{-/-}$ RPE. Scale bars = 1 μm.

test the phagocytotic activity of cultured RPE cells (52). The OS vesicles were not always intact when isolated, especially those from $Nrl^{-/-}$ animals, due to interconnections of the cone-like discs, and thus would produce membranes with PS exposed to RPE cells that would promote normal phagocytosis. Signals were noted to emanate selectively from OS membrane vesicles that had been ingested by the RPE rather than any other source (**Fig. 6*A–C***). *Wt* RPE cells, when challenged with OS from *Wt* mice, phagocytosed these membranes as expected (Fig. 6*D–F*). Ingestion of OS membranes by the RPE was also confirmed by TEM imaging of thin plastic blocks (Supplemental Fig. S3*C, D*). When the *Wt* RPE cells were challenged with OS from $Nrl^{-/-}$ mice, the RPE phagocytosed these membranes as well (Fig. 6*G, I*). Moreover, RPE cells cultured from $Nrl^{-/-}$ mice also phagocytosed OS from *Wt* mice (Fig. 6*J, L*) as well as from $Nrl^{-/-}$ animals (Fig. 6*M, O*). These results indicate that the $Nrl^{-/-}$defect was not in the RPE, but rather it is related to photoreceptors and their interface with the RPE.

DISCUSSION

The details of abnormal photoreceptor development resulting from mutations in *NR2E3* and *NRL* genes have captured the interest of developmental biologists for nearly 2 decades. However, an equally important but less explored feature of ESCS is the progressive retinal degeneration that leads to blindness in these patients (6, 7, 15, 82). Retinal degeneration in ESCS has been postulated to be secondary to a defective photoreceptor maintenance function of NR2E3 or a combination of cell proliferation and death (14, 15, 55), but specifics have been lacking. To understand this unique human condition, an appropriate animal model is required. Knockout of the *Nrl* transcription factor in mice produces a retina that is overpopulated with S-cone-like photoreceptors along with a complete absence of rod photoreceptors. Morphological assessment of this $Nrl^{-/-}$ mouse model revealed that the postnatal perturbation of retinal organization (12, 83, 84) was similar to the disorganized retinal layering noted in postmortem donor retinas of patients with ESCS (14, 15). In this study, by comparing and following patients with ESCS, we show by *in vivo* and *ex vivo* imaging that the $Nrl^{-/-}$ mouse model approximates the phenotypic features of human ESCS. Thus, the $Nrl^{-/-}$ mouse model allowed us to probe the molecular mechanisms of ESCS-induced retinal degeneration.

Comprehensive analysis of the murine eye and retina transcriptomes of *Wt* and $Nrl^{-/-}$ mice by RNA-Seq allowed greater understanding of the global transcrip-

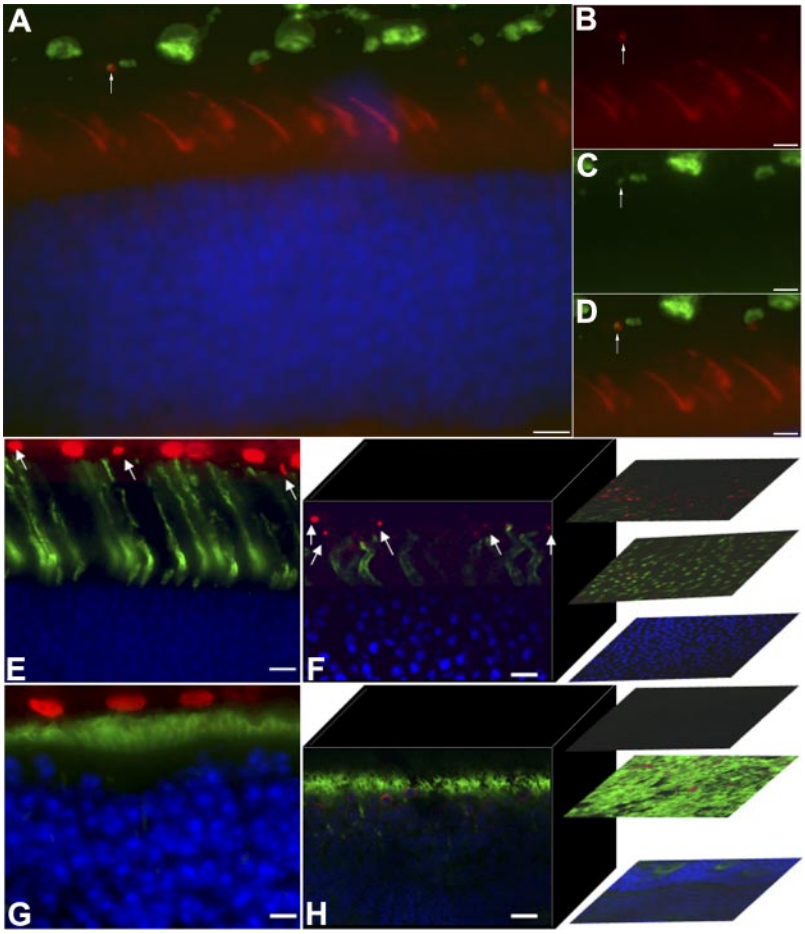

Figure 5. Absent phagosome staining at the photoreceptor-RPE interface confirms impaired phagocytosis in *Nrl*$^{-/-}$ mice. Absence of proper phagocytosis was confirmed by biochemical staining for phosphatidylserine (PS) found on phagosomes and its localization with shed cone disc packets. *A*) In *Wt* retina, shed cone opsin discs (red; cone opsin antibody) colocalize with phagosomes stained for PS (green; indicated by arrow) at the photoreceptor-RPE interface. (Note that not all the PS staining indicates phagosomes as PS dye also stains the RPE cell nucleus). B–D) Zoom views show a cone opsin disc (red; indicated by arrow; *B*), PS phagsome staining (green; indicated by arrow; *C*), and colocalization of the two stains (indicated by arrow; *D*). *E*) In samples of *Wt* mouse retina examined at the peak of phagocytosis, staining of phagosomes (red) was found at the photoreceptor-RPE interface (arrows). *F*) Through optical sectioning of the collected data, confocal imaging of the retina-RPE interface reveals that the PS signal is present at the photoreceptor-RPE interface. Still image of the tangential plane of these collected data shows 3 corresponding slices of data at right, indicating layers containing nuclear (blue), cone sheath (green), and phagosome (red) signals. *G*) In contrast, comparable *Nrl*$^{-/-}$ retinal samples fail to exhibit staining for PS at the photoreceptor-RPE interface. *H*) Confocal imaging of the *Nrl*$^{-/-}$ retina-RPE interface shows that no detectable PS signal is evident at the photoreceptor-RPE interface. Note that it appears that there is some PS staining in the *Nrl*$^{-/-}$ retina, but it is not located at the interface. Still image of the tangential plane of the collected data shows 3 slices of data at right, indicating layers containing nuclear (blue), ESCS photoreceptor (green), and phagosome (red) signals. Staining: cone opsin for cone OS; PNA for cone sheaths; DAPI or Topro 3 nuclear stain; phosphatidylserine for phagosomes. Scale bars = 5 μm.

tional misregulation that results in aberrant, unstable photoreceptors of the *Nrl*$^{-/-}$ mouse retina. Interestingly, our RNA-Seq analysis reveals that many signaling networks, such as Notch and Hedgehog, needed for normal photoreceptor maintenance and retinal lamination are misregulated in *Nrl*$^{-/-}$mice. Proper retinal cell type specification is heavily reliant on both Notch (17, 85) and Hedgehog signaling (69, 70), because depletion or pharmacological inhibition of *Notch1* or *Dhh* in the retina causes progenitor cells to differentiate prematurely. Notably, *Notch1* inhibition causes commitment of retinal progenitor cells to a cone photoreceptor fate, preferentially specifying S cones (17, 18, 86). Furthermore, both *Notch1* and *Dhh* are critical for proper retinal morphology, as their depletion in the retina causes rosette formation in the ONL (58, 87, 88). Precocious S-cone formation and ONL rosette formation resulting from aberrations in Notch and Hedgehog in the retina are consistent with what is observed in the mature *Nrl*$^{-/-}$ retina.

The misregulation of Hedgehog and Notch pathways is evident by almost complete absence of *Dhh* in *Nrl*$^{-/-}$ retina compared to *Wt* and up-regulation of bHLH factors in *Nrl*$^{-/-}$ retina. The latter are normally suppressed by proper Notch signaling. Examples include neurogenic differentiation 1 (*NeuroD1*) and *Atoh7*, genes responsible for committing cells to the earliest cell fates of S-cone photoreceptors and ganglion cells, respectively. *NeuroD1* alone cannot commit cells to the S-cone fate, but can do so in cooperation with *Six6*, another transcript up-regulated in the *Nrl*$^{-/-}$ retina. *Six6* can be activated by *NeuroD1* (89). Further, *Eya1*, in the pathway of canonical Pax signaling, is another transcript highly elevated in the *Nrl*$^{-/-}$retina. Although elevated levels of *NeuroD1* and *Six6* can commit cells to a S-cone fate, a prolonged increase of *Six6* expression leads to disruption of photoreceptor maturation, indicating a regulatory factor is needed to down-regulate *Six6* activity after its induction (89). We hypothesize that the regulatory factor that could control terminal photoreceptor differentiation in this pathway is sine oculis-related homeobox 6 homologue opposite strand transcript 1 (*Six6os1*), which is highly up-regulated in the *Nrl*$^{-/-}$ eye and retina (Fig. 2*F* and **Fig. 7*A***). Opposite strand transcripts are natural antisense transcripts that can be involved in gene regulation, and recently, it was predicted that both *Six6os1* and *Crxos1* might encode putative protein products and thereby play a major role in photoreceptor development (90). Altogether, RNA-Seq based elucidation of the eye and

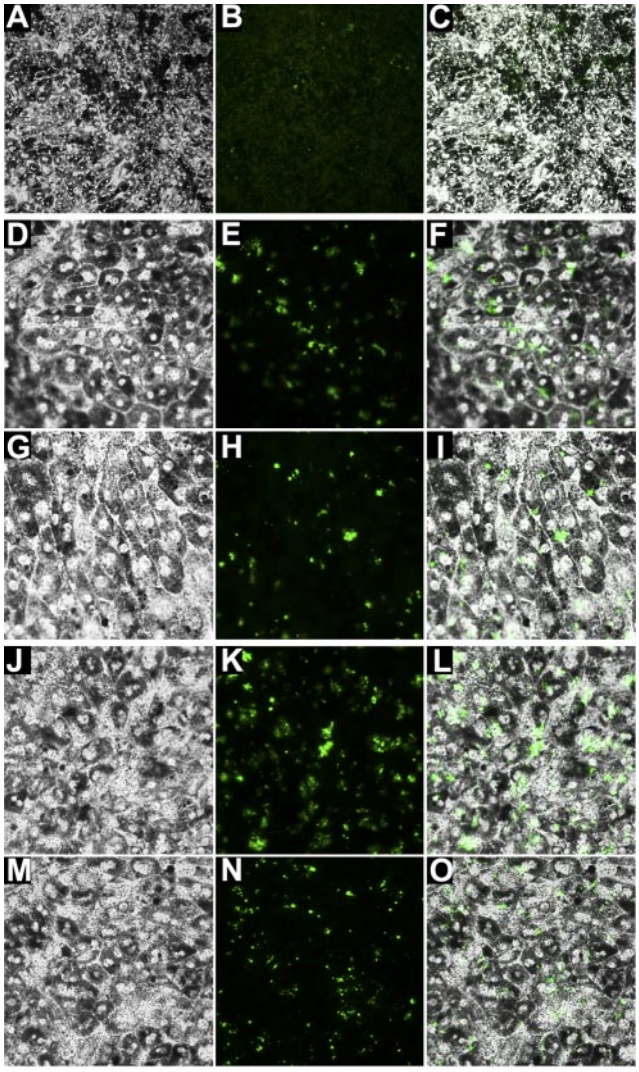

Figure 6. Wt and $Nrl^{-/-}$ mouse RPE phagocytose both *Wt* and $Nrl^{-/-}$ photoreceptor OS membranes. First, the phagocytosis assay was run with no OSs as a negative control. *A–C*) *Wt* mouse RPE cells in culture not subjected to photoreceptor challenge (*A*) were just washed with FITC-labeled dye (*B*) where only faint background fluorescence was detected; images were overlaid (*C*). *D–F*) *Wt* RPE cells (*D*) were challenged with isolated *Wt* photoreceptor OS membranes (*E*); phagocytosis of the OS membranes was seen in the overlapping images (*F*). *G–I*) *Wt* RPE cells (*G*) challenged with isolated $Nrl^{-/-}$ photoreceptor OS membranes (*H*) phagocytosed the OS membranes, as evident in the overlapping images (*I*). *J–L*) $Nrl^{-/-}$ RPE cells (*J*) challenged with isolated *Wt* photoreceptor OS membranes (*K*) phagocytosed the OS membranes, as evident in the overlapping image (*L*). *M–O*) Similarly, $Nrl^{-/-}$ RPE (*M*) challenged with isolated $Nrl^{-/-}$ photoreceptor OS membranes (*N*) phagocytosed the OS membranes, as evident in the overlapping images (*O*).

retinal transcriptomes revealed transcriptional mis-regulation in the mature $Nrl^{-/-}$ mice. These factors along with others identified in this study can potentially play a crucial role in cone photoreceptor maintenance (Fig. 7*B*). Indeed, proteins encoded by those unique genes found from this study to have no annotated function could prove especially attractive candidates for this role.

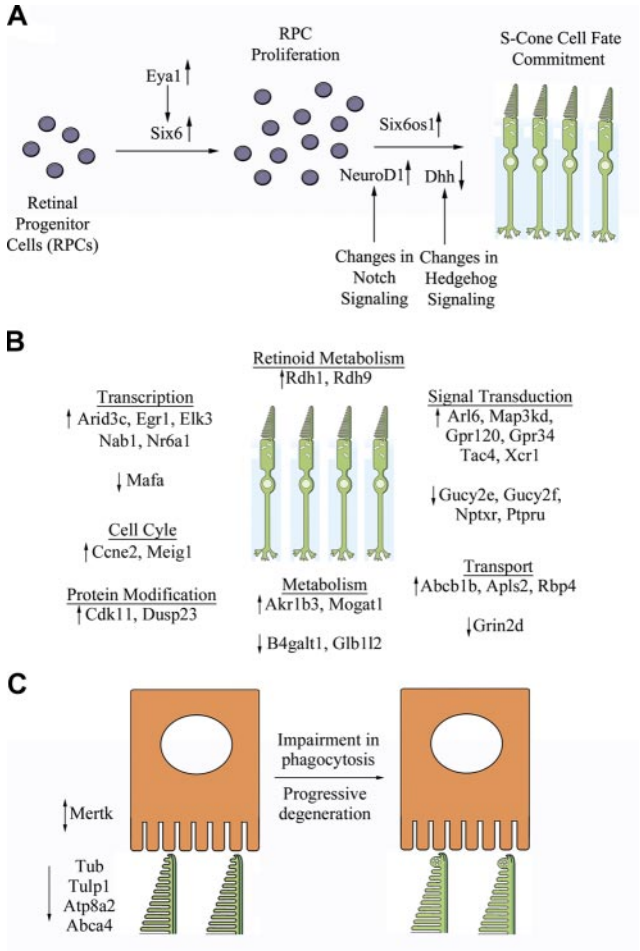

Figure 7. Transcriptional misregulation causes precocious development of cone-like cells in the $Nrl^{-/-}$ retina, which are then maintained by transcriptional networks that alter key homeostatic processes. *A*) Increased levels of *Eya1* in the $Nrl^{-/-}$ retina can activate the expression of *Six6*, which causes retinal progenitor cell (RPC) proliferation. Commitment of these retinal cells to an early cell fate requires a premature cell cycle exit. This is mediated by altered levels of Notch and Hedgehog transcriptional networks that produce increased levels of *NeuroD1* and decreased levels of *Dhh* in the $Nrl^{-/-}$ retina. *Six6* and *NeuroD1* together with *Six6os1*, exercising a possible regulatory role on *Six6*, synergize to promote the S-cone fate rather than alternative early cell fates. *B*) Maintenance of the cone-like cells in the mature retina can be attributed to a series of genes involved in transcriptional control of retinoid metabolism, transport, cell cycling, and signal transduction. Unique transcripts identified by RNA-Seq to be ≥5-fold differentially expressed in $Nrl^{-/-}$ *vs. Wt* mouse retina provide a resource for identifying maintenance factors required for cone cell survival and the alterations that accompany disease. Up and down arrows indicate transcripts that are up- and down-regulated, respectively, in $Nrl^{-/-}$ *vs. Wt* retina, as determined by RNA-Seq. *C*) Transcriptional misregulation causes changes in the expression of key homeostatic genes involved in phagocytosis, leading to the pathological degeneration in ESCS. The most critical receptor tyrosine kinase, *Mertk*, involved in RPE phagocytosis is unchanged in the $Nrl^{-/-}$ retina compared to *Wt*. However, key homeostatic genes involved in photoreceptor OS phagocytosis and toxic metabolic movement, such as *Abca4*, *Atp8a2*, *Tub*, *Tulp1*, are down-regulated in the $Nrl^{-/-}$ retina compared to *Wt*, thus contributing to the defect in photoreceptor phagocytosis. Down arrows indicate transcripts that are down-regulated in the $Nrl^{-/-}$ retina compared to *Wt*; the up/down arrow indicates transcripts that were unchanged in expression, as determined by RNA-Seq.

Although the RNA-Seq study identified transcriptional mis-regulation that could affect normal cone photoreceptor maintenance, it also provided a potential molecular mechanism for ESCS induced retinal degeneration due to defective photoreceptor phagocytosis. RNA-Seq revealed down-regulation of genes involved in photoreceptor phagocytosis, such as tubby (*Tub*) and tubby-like protein 1 (*Tulp1*) (77) and possibly a recently described PS flippase in photoreceptor disc membranes, *Atp8a2* (91). This prompted a more detailed study of the photoreceptor-RPE interface with high-resolution imaging methods. Compared to *Wt* rods correctly apposed at the RPE interface, ESCS photoreceptors examined by TEM demonstrated abnormal interactions with the RPE. Phagocytotic material shed from OS could not be detected across the retinas of multiple $Nrl^{-/-}$ animals. Instead, the OS layer displayed a buildup of vacuole-like material in the heads of the photoreceptor (Fig. 3*P*, *R*), likely accounting for the bulbous OS head structures identified by SEM imaging (Fig. 3*K*, *L*). This phenotype changed with increasing age such that the OS became devoid of discs. Thin sections also supported this view. However, such data do not illustrate the dynamic process of phagocytosis across the retina. Phagosomes could be lacking in any given section, because only ~10% of photoreceptors may be shedding at any one time. Therefore, we used SBF-SEM to section through an entire RPE cell in contact with hundreds of photoreceptor cells. This strategy allowed all phagocytotic events to be identified in *Wt* mouse retina at the morning peak of phagocytosis. In contrast, when the $Nrl^{-/-}$ retina was studied using the same approach, no phagosomes were detected. This apparent defect in phagocytosis was then validated biochemically. Retinas from *Wt* mice stained with phagosomal markers, such as PS and annexin V, exhibited phagosomes at the photoreceptor-RPE interface. There was a complete absence of such staining in $Nrl^{-/-}$ mouse retina. Thus, both the defect in phagocytosis and the degenerative component of ESCS seem attributable to aberrant photoreceptors in the retina rather than a combination of photoreceptor and RPE cell dysfunction. This was consistent with the RNA-Seq study where the critical receptor tyrosine kinase involved in phagocytosis, *Mertk*, was unchanged at the transcriptional level between *Wt* and $Nrl^{-/-}$ mice. The aberrant photoreceptor hypothesis was further supported by challenging cultured *Wt* and $Nrl^{-/-}$ RPE cells with OS membranes. In the challenge assay, the fed OSs are not intact and thus broken pieces presenting PS will readily be phagocytosed by the RPE cells. Both *Wt* and $Nrl^{-/-}$ RPE cells revealed comparable phagocytotic activity, indicating that the defect in phagocytosis was independent of an impairment in RPE function. Instead, the aberrant packing and spacing of the photoreceptors in ESCS disrupts the normal phagocytosis machinery of shed photoreceptor discs.

Based on this phagocytotic defect found in $Nrl^{-/-}$ mice, we hypothesize that it is the precipitating cause of the retinal degeneration that occurs in human and murine ESCS (Fig. 7*C*). Previous investigators have speculated that retinal degeneration in ESCS is secondary to a postnatal photoreceptor maintenance function of *NR2E3*, for example (15, 92). However, the dysplasia in human ESCS and murine models, evidenced by rosettes (or whorls), is not unique to ESCS but is a feature of many retinal pathological processes (93). Patchy loss of laminar integrity and abnormal photoreceptor-RPE interactions are dramatic features accompanying the rosettes in many diseases, but no direct evidence indicates that this causes progressive retinal degeneration. Even the hypothesis that overcrowding due to retinal folding or rosette formations may be relieved by photoreceptor degeneration has been disputed (93). Phagocytosis of shed disc packets from the OS of photoreceptors is essential for normal function of these cells (3). Without this process, the buildup of material becomes toxic to the cell over time as demonstrated in the Royal College of Surgeons rat, which is defective for *Mertk* (94, 95). Similarly, impairment of phagocytosis in the $Nrl^{-/-}$ retina could progressively cause a buildup of toxic materials that leads to degeneration. This buildup of toxic compounds would produce a fluorescent signal in the retina, much like the one we identified in patients with ESCS (Fig. 1*E*).

In summary, we have shown that photoreceptors in the $Nrl^{-/-}$ retina have robust expression of S-cone opsin and they display an aberrant packing and morphology leading to progressive degeneration attributable to a defect in normal photoreceptor phagocytosis. Changes in the transcriptional landscape of the $Nrl^{-/-}$ eye result in the expression of a unique subset of photoreceptor genes at levels that differ from those of native rods or cones. The developmental defect that affects photoreceptor cell fate also appears to have a detrimental effect on the normal retinal microenvironment. Thus, the inherent defect in phagocytosis in the $Nrl^{-/-}$ retina observed in this work is likely caused by changes in the normal transcriptional landscape that causes an overpopulation of ESCS photoreceptors in the retina. In animals, such as the tree shrew, that possess retinas that are almost completely populated with cones, phagocytosis occurs normally (5). The produced mutant photoreceptor cells in ESCS have a lower density than photoreceptor cells in *Wt* rod or cone-dominated retina as well as disruption in expression of key homeostatic genes, including genes involved in proper photoreceptor phagocytosis and maintenance. This could account for their instability. These changes make ESCS photoreceptors unstable, producing retinal degeneration at an early age. FJ

The authors thank Dr. Anand Swaroop (National Eye Institute) for helpful discussions and Dr. Leslie T. Webster Jr., Dr. Yoshikazu Imanishi, Dr. Michael E. Maguire and Dr. Akiko Maeda (Case Western Reserve University) for valuable comments about the manuscript. The authors thank Dr. Russell Van Gelder (University of Washington, Seatttle, WA, USA) for providing the scanning electron microscope for imaging and Dr. David Williams and Dr. Tanja Diemer

(University of California, Los Angeles, CA, USA) for graciously offering to demonstrate their RPE isolation technique. The authors also thank Dr. Yan Liang, Dr. Hisashi Fujioka, Dr. Heather Holdaway, Dr. Glenn Lobo, Neil Molyneaux, Satsumi Roos, Simone Edelheit, Pamela Supelak, Sungho Lee (Case Western Reserve University), and Christopher Bleck (University of Basel, Basel, Switzerland) for sample preparation, imaging assistance, data analysis help and useful discussions. This research was supported by U.S. National Institutes of Health (NIH) grants EY009339 and EY019478, and by a grant from Foundation Fighting Blindness. D.M. was supported in part by Case Western Reserve University (CWRU) Medical Scientist Training Program grant T32 GM007250 from NIH, Visual Sciences Training grant T32 EY007157 from NIH, and the Maurice E. Müller Foundation of Switzerland. B.M.K. was supported by a CWRU Department of Nutrition Metabolic Training grant postdoctoral fellowship award from National Institute of Diabetes and Digestive and Kidney Diseases grant DK-007319. K.P. is John H. Hord Professor of Pharmacology.

REFERENCES

1. Livesey, F. J., and Cepko, C. L. (2001) Vertebrate neural cell-fate determination: lessons from the retina. *Nat. Rev. Neurosci.* **2,** 109–118
2. Swaroop, A., Kim, D., and Forrest, D. (2010) Transcriptional regulation of photoreceptor development and homeostasis in the mammalian retina. *Nat. Rev. Neurosci.* **11,** 563–576
3. Kevany, B. M., and Palczewski, K. (2010) Phagocytosis of retinal rod and cone photoreceptors. *Physiology* **25,** 8–15
4. Anderson, D. H., Fisher, S. K., and Steinberg, R. H. (1978) Mammalian cones: disc shedding, phagocytosis, and renewal. *Invest. Ophthalmol. Vis. Sci.* **17,** 117–133
5. Immel, J. H., and Fisher, S. K. (1985) Cone photoreceptor shedding in the tree shrew (tupaia-belangerii). *Cell Tissue Res.* **239,** 667–675
6. Jacobson, S. G., Marmor, M. F., Kemp, C. M., and Knighton, R. W. (1990) Sws (Blue) cone hypersensitivity in a newly identified retinal degeneration. *Invest. Ophthalmol. Visual Sci.* **31,** 827–838
7. Jacobson, S. G., Roman, A. J., Roman, M. I., Gass, J. D. M., and Parker, J. A. (1991) Relatively enhanced S-cone function in the Goldmann-Favre syndrome. *Am. J. Ophthalmol.* **111,** 446–453
8. Hood, D. C., Cideciyan, A. V., Roman, A. J., and Jacobson, S. G. (1995) Enhanced S-cone-syndrome - evidence for an abnormally large number of S-cones. *Vision Res.* **35,** 1473–1481
9. Haider, N. B., Jacobson, S. G., Cideciyan, A. V., Swiderski, R., Streb, L. M., Searby, C., Beck, G., Hockey, R., Hanna, D. B., Gorman, S., Duhl, D., Carmi, R., Bennett, J., Weleber, R. G., Fishman, G. A., Wright, A. F., Stone, E. M., and Sheffield, V. C. (2000) Mutation of a nuclear receptor gene, NR2E3, causes enhanced S cone syndrome, a disorder of retinal cell fate. *Nat. Genet.* **24,** 127–131
10. Nishiguchi, K. M., Friedman, J. S., Sandberg, M. A., Swaroop, A., Berson, E. L., and Dryja, T. P. (2004) Recessive NRL mutations in patients with clumped pigmentary retinal degeneration and relative preservation of blue cone function. *Proc. Natl. Acad. Sci. U. S. A.* **101,** 17819–17824
11. Wright, A. F., Reddick, A. C., Schwartz, S. B., Ferguson, J. S., Aleman, T. S., Kellner, U., Jurklies, B., Schuster, A., Zrenner, E., Wissinger, B., Lennon, A., Shu, X., Cideciyan, A. V., Stone, E. M., Jacobson, S. G., and Swaroop, A. (2004) Mutation analysis of NR2E3 and NRL genes in enhanced S cone syndrome. *Hum. Mutat.* **24,** 439
12. Mears, A. J., Kondo, M., Swain, P. K., Takada, Y., Bush, R. A., Saunders, T. L., Sieving, P. A., and Swaroop, A. (2001) Nrl is required for rod photoreceptor development. *Nat. Genetics* **29,** 447–452
13. Yetemian, R. M., Brown, B. M., and Craft, C. M. (2010) Neovascularization, enhanced inflammatory response, and age-related cone dystrophy in the Nrl(−/−) Grk1(−/−) mouse retina. *Invest. Ophthalmol. Vis. Sci.* **51,** 6196–6206
14. Bonilha, V. L., Fishman, G. A., Rayborn, M. E., and Hollyfield, J. G. (2009) Retinal pathology of a patient with Goldmann-Favre syndrome. *Ophthalmic Genet.* **30,** 172–180
15. Milam, A. H., Rose, L., Cideciyan, A. V., Barakat, M. R., Tang, W. X., Gupta, N., Aleman, T. S., Wright, A. F., Stone, E. M., Sheffield, V. C., and Jacobson, S. G. (2002) The nuclear receptor NR2E3 plays a role in human retinal photoreceptor differentiation and degeneration. *Proc. Natl. Acad. Sci. U. S. A.* **99,** 473–478
16. Mustafi, D., Avishai, A., Avishai, N., Engel, A., Heuer, A., and Palczewski, K. (2011) Serial sectioning for examination of photoreceptor cell architecture by focused ion beam technology. *J. Neurosci. Methods* **198,** 70–76
17. Jadhav, A. R., Mason, H. A., and Cepko, C. L. (2006) Notch 1 inhibits photoreceptor production in the developing mammalian retina. *Development* **133,** 913–923
18. Yaron, O., Farhy, C., Marquardt, T., Applebury, M., and Ashery-Padan, R. (2006) Notch1 functions to suppress cone-photoreceptor fate specication in the developing mouse retina. *Development* **133,** 1367–1378
19. Wall, D. S., Mears, A. J., McNeill, B., Mazerolle, C., Thurig, S., Wang, Y. P., Kageyama, R., and Wallace, V. A. (2009) Progenitor cell proliferation in the retina is dependent on Notch-independent Sonic hedgehog/Hes1 activity. *J. Cell Biol.* **184,** 101–112
20. Velculescu, V. E., Zhang, L., Vogelstein, B., and Kinzler, K. W. (1995) Serial analysis of gene expression. *Science* **270,** 484–487
21. Blackshaw, S., Fraioli, R. E., Furukawa, T., and Cepko, C. L. (2001) Comprehensive analysis of photoreceptor gene expression and the identification of candidate retinal disease genes. *Cell* **107,** 579–589
22. Blackshaw, S., Harpavat, S., Trimarchi, J., Cai, L., Huang, H., Kuo, W. P., Weber, G., Lee, K., Fraioli, R. E., Cho, S. H., Yung, R., Asch, E., Ohno-Machado, L., Wong, W. H., and Cepko, C. L. (2004) Genomic analysis of mouse retinal development. *PLoS Biol.* **2,** E247
23. Sharon, D., Blackshaw, S., Cepko, C. L., and Dryja, T. P. (2002) Profile of the genes expressed in the human peripheral retina, macula, and retinal pigment epithelium determined through serial analysis of gene expression (SAGE). *Proc. Natl. Acad. Sci. U. S. A.* **99,** 315–320
24. Adams, M. D., Kelley, J. M., Gocayne, J. D., Dubnick, M., Polymeropoulos, M. H., Xiao, H., Merril, C. R., Wu, A., Olde, B., Moreno, R. F., Kerlavage, A. R., McCombie, W. R., and Venter, J. C. (1991) Complementary DNA sequencing: expressed sequence tags and human genome project. *Science* **252,** 1651–1656
25. Yu, J., Farjo, R., MacNee, S. P., Baehr, W., Stambolian, D. E., and Swaroop, A. (2003) Annotation and analysis of 10,000 expressed sequence tags from developing mouse eye and adult retina. *Genome Biol.* **4,** R65
26. Yoshida, S., Mears, A. J., Friedman, J. S., Carter, T., He, S., Oh, E., Jing, Y. Z., Farjo, R., Fleury, G., Barlow, C., Hero, A. O., and Swaroop, A. (2004) Expression profiling of the developing and mature Nrl(−/−) mouse retina: identification of retinal disease candidates and transcriptional regulatory targets of Nrl. *Human Mol. Genetics* **13,** 1487–1503
27. Corbo, J. C., and Cepko, C. L. (2005) A hybrid photoreceptor expressing both rod and cone genes in a mouse model of enhanced S-cone syndrome. *PLoS Genet.* **1,** e11
28. Corbo, J. C., Myers, C. A., Lawrence, K. A., Jadhav, A. P., and Cepko, C. L. (2007) A typology of photoreceptor gene expression patterns in the mouse. *Proc. Natl. Acad. Sci. U. S. A.* **104,** 12069–12074
29. Denoeud, F., Aury, J. M., Da Silva, C., Noel, B., Rogier, O., Delledonne, M., Morgante, M., Valle, G., Wincker, P., Scarpelli, C., Jaillon, O., and Artiguenave, F. (2008) Annotating genomes with massive-scale RNA sequencing. *Genome Biol.* **9,** R175
30. Wang, Z., Gerstein, M., and Snyder, M. (20) RNA-Seq: a revolutionary tool for transcriptomics. *Nat. Rev. Genet.* **10,** 57–63
31. Han, X. W., Wu, X., Chung, W. Y., Li, T., Nekrutenko, A., Altman, N. S., Chen, G., and Ma, H. (2009) Transcriptome of embryonic and neonatal mouse cortex by high-throughput RNA sequencing. *Proc. Natl. Acad. Sci. U. S. A.* **106,** 12741–12746
32. Wu, J. Q., Habegger, L., Noisa, P., Szekely, A., Qiu, C. H., Hutchison, S., Raha, D., Egholm, M., Lin, H. F., Weissman, S., Cui, W., Gerstein, M., and Snyder, M. (2010) Dynamic transcrip-

tomes during neural differentiation of human embryonic stem cells revealed by short, long, and paired-end sequencing. *Proc. Natl. Acad. Sci. U. S. A.* **107,** 5254–5259
33. Nagalakshmi, U., Wang, Z., Waern, K., Shou, C., Raha, D., Gerstein, M., and Snyder, M. (2008) The transcriptional landscape of the yeast genome defined by RNA sequencing. *Science* **320,** 1344–1349
34. Denk, W., and Horstmann, H. (2004) Serial block-face scanning electron microscopy to reconstruct three-dimensional tissue nanostructure. *PLoS Biol.* **2,** 1900–1909
35. Rouquette, J., Genoud, C., Vazquez-Nin, G. H., Kraus, B., Cremer, T., and Fakan, S. (2009) Revealing the high-resolution three-dimensional network of chromatin and interchromatin space: A novel electron-microscopic approach to reconstructing nuclear architecture. *Chromosome Res.* **17,** 801–810
36. MacKenzie, D., Arendt, A., Hargrave, P., McDowell, J. H., and Molday, R. S. (1984) Localization of binding sites for carboxyl terminal specific anti-rhodopsin monoclonal antibodies using synthetic peptides. *Biochemistry* **23,** 6544–6549
37. Jacobson, S. G., Yagasaki, K., Feuer, W. J., and Roman, A. J. (1989) Interocular asymmetry of visual function in heterozygotes of X-linked retinitis pigmentosa. *Exp. Eye Res.* **48,** 679–691
38. Aleman, T. S., Cideciyan, A. V., Sumaroka, A., Windsor, E. A., Herrera, W., White, D. A., Kaushal, S., Naidu, A., Roman, A. J., Schwartz, S. B., Stone, E. M., and Jacobson, S. G. (2008) Retinal laminar architecture in human retinitis pigmentosa caused by rhodopsin gene mutations. *Invest. Ophthalmol. Vis. Sci.* **49,** 1580–1590
39. Cideciyan, A. V., Aleman, T. S., Boye, S. L., Schwartz, S. B., Kaushal, S., Roman, A. J., Pang, J. J., Sumaroka, A., Windsor, E. A., Wilson, J. M., Flotte, T. R., Fishman, G. A., Heon, E., Stone, E. M., Byrne, B. J., Jacobson, S. G., and Hauswirth, W. W. (2008) Human gene therapy for RPE65 isomerase deficiency activates the retinoid cycle of vision but with slow rod kinetics. *Proc. Natl. Acad. Sci. U. S. A.* **105,** 15112–15117
40. Huang, Y., Cideciyan, A. V., Papastergiou, G. I., Banin, E., Semple-Rowland, S. L., Milam, A. H., and Jacobson, S. G. (1998) Relation of optical coherence tomography to microanatomy in normal and rd chickens. *Invest. Ophthalmol. Vis. Sci.* **39,** 2405–2416
41. Jacobson, S. G., Aleman, T. S., Sumaroka, A., Cideciyan, A. V., Roman, A. J., Windsor, E. A., Schwartz, S. B., Rehm, H. L., and Kimberling, W. J. (2009) Disease boundaries in the retina of patients with Usher syndrome caused by MYO7A gene mutations. *Invest. Ophthalmol. Vis. Sci.* **50,** 1886–1894
42. Cideciyan, A. V., Swider, M., Aleman, T. S., Roman, M. I., Sumaroka, A., Schwartz, S. B., Stone, E. M., and Jacobson, S. G. (2007) Reduced-illuminance autofluorescence imaging in ABCA4-associated retinal degenerations. *J. Opt. Soc. Am. A.* **24,** 1457–1467
43. Drexler, W., and Fujimoto, J. G. (2008) State-of-the-art retinal optical coherence tomography. *Prog. Retin. Eye Res.* **27,** 45–88
44. Wang, W. H., McNatt, L. G., Shepard, A. R., Jacobson, N., Nishimura, D. Y., Stone, E. M., Sheffield, V. C., and Clark, A. F. (2001) Optimal procedure for extracting RNA from human ocular tissues and expression profiling of the congenital glaucoma gene FOXC1 using quantitative RT-PCR. *Mol. Vis.* **7,** 89–94
45. Hsu, F., Kent, W. J., Clawson, H., Kuhn, R. M., Diekhans, M., and Haussler, D. (2006) The UCSC known genes. *Bioinformatics* **22,** 1036–1046
46. Batten, M. L., Imanishi, Y., Maeda, T., Tu, D. C., Moise, A. R., Bronson, D., Possin, D., Van Gelder, R. N., Baehr, W., and Palczewski, K. (2004) Lecithin-retinol acyltransferase is essential for accumulation of all-trans-retinyl esters in the eye and in the liver. *J. Biol. Chem.* **279,** 10422–10432
47. Imanishi, Y., Gerke, V., and Palczewski, K. (2004) Retinosomes: new insights into intracellular managing of hydrophobic substances in lipid bodies. *J. Cell Biol.* **166,** 447–453
48. Bray, D. F., Bagu, J., and Koegler, P. (1993) Comparison of hexamethyldisilazane (HMDS), Peldri II, and critical-point drying methods for scanning electron microscopy of biological specimens. *Microsc. Res. Tech.* **26,** 489–495
49. Fiala, J. C. (2005) Reconstruct: a free editor for serial section microscopy. *J. Microsc.* **218,** 52–61
50. Diemer, T., Gibbs, D., and Williams, D. S. (2008) Analysis of the rate of disk membrane digestion by cultured RPE cells. *Adv. Exp. Med. Biol.* **613,** 321–326
51. Liang, Y., Fotiadis, D., Filipek, S., Saperstein, D. A., Palczewski, K., and Engel, A. (2003) Organization of the G protein-coupled receptors rhodopsin and opsin in native membranes. *J. Biol. Chem.* **278,** 21655–21662
52. Finnemann, S. C., Bonilha, V. L., Marmorstein, A. D., and RodriguezBoulan, E. (1997) Phagocytosis of rod outer segments by retinal pigment epithelial cells requires alpha v beta 5 integrin for binding but not for internalization. *Proc. Natl. Acad. Sci. U. S. A.* **94,** 12932–12937
53. Roman, A. J., and Jacobson, S. G. (1991) S-cone-driven but not S-cone-type electroretinograms in the enhanced S-cone syndrome. *Exp. Eye Res.* **53,** 685–690
54. Roman, A. J., and Jacobson, S. G. (1991) Response properties of the S (Blue) cone-mediated Erg in the enhanced S cone syndrome. *Invest. Ophthalmol. Vis. Sci.* **32,** 1138–1138
55. Jacobson, S. G., Sumaroka, A., Aleman, T. S., Cideciyan, A. V., Schwartz, S. B., Roman, A. J., McInnes, R. R., Sheffield, V. C., Stone, E. M., Swaroop, A., and Wright, A. F. (2004) Nuclear receptor NR2E3 gene mutations distort human retinal laminar architecture and cause an unusual degeneration. *Hum. Mol. Genet.* **13,** 1893–1902
56. Curcio, C. A., Allen, K. A., Sloan, K. R., Lerea, C. L., Hurley, J. B., Klock, I. B., and Milam, A. H. (1991) Distribution and morphology of human cone photoreceptors stained with anti-blue opsin. *J. Comp. Neurol.* **312,** 610–624
57. Delori, F. C., Dorey, C. K., Staurenghi, G., Arend, O., Goger, D. G., and Weiter, J. J. (1995) In-vivo fluorescence of the ocular fundus exhibits retinal-pigment epithelium lipofuscin characteristics. *Invest. Ophthalmol. Vis. Sci.* **36,** 718–729
58. Wenzel, A., von Lintig, J., Oberhauser, V., Tanimoto, N., Grimm, C., and Seeliger, M. W. (2007) RPE65 is essential for the function of cone photoreceptors in NRL-deficient mice. *Invest. Ophthalmol. Vis. Sci.* **48,** 534–542
59. Luhmann, U. F. O., Robbie, S., Munro, P. M. G., Barker, S. E., Duran, Y., Luong, V., Fitzke, F. W., Bainbridge, J. W. B., Ali, R. R., and MacLaren, R. E. (2009) The Drusenlike phenotype in aging Ccl2-knockout mice is caused by an accelerated accumulation of swollen autofluorescent subretinal macrophages. *Invest. Ophthalmol. Vis. Sci.* **50,** 5934–5943
60. Wang, N. K., Fine, H. F., Chang, S., Chou, C. L., Cella, W., Tosi, J., Lin, C. S., Nagasaki, T., and Tsang, S. H. (2009) Cellular origin of fundus autofluorescence in patients and mice with a defective NR2E3 gene. *Br. J. Ophthalmol.* **93,** 1234–1240
61. Brown, N. L., Patel, S., Brzezinski, J., and Glaser, T. (2001) Math5 is required for retinal ganglion cell and optic nerve formation. *Development* **128,** 2497–2508
62. Kawakami, K., Sato, S., Ozaki, H., and Ikeda, K. (2000) Six family genes—structure and function as transcription factors and their roles in development. *Bioessays* **22,** 616–626
63. Kumar, J. P. (2009) The sine oculis homeobox (SIX) family of transcription factors as regulators of development and disease. *Cell. Mol. Life Sci.* **66,** 565–583
64. Chen, R., Amoui, M., Zhang, Z. H., and Mardon, G. (1997) Dachshund and eyes absent proteins form a complex and function synergistically to induce ectopic eye development in *Drosophila*. *Cell* **91,** 893–903
65. Ikeda, K., Watanabe, Y., Ohto, H., and Kawakami, K. (2002) Molecular interaction and synergistic activation of a promoter by Six, Eya, and Dach proteins mediated through CREB binding protein. *Mol. Cell. Biol.* **22,** 6759–6766
66. Pignoni, F., Hu, B. R., Zavitz, K. H., Xiao, J. A., Garrity, P. A., and Zipursky, S. L. (1997) The eye-specification proteins so and eya form a complex and regulate multiple steps in *Drosophila* eye development. *Cell* **91,** 881–891
67. Gehring, W. J. (2002) The genetic control of eye development and its implications for the evolution of the various eye-types. *Int. J. Dev. Biol.* **46,** 65–73
68. Gehring, W. J. (2005) New perspectives on eye development and the evolution of eyes and photoreceptors. *J. Hered.* **96,** 171–184
69. Sakagami, K., Gan, L., and Yang, X. J. (2009) Distinct effects of hedgehog signaling on neuronal fate specification and cell cycle progression in the embryonic mouse retina. *J. Neurosci.* **29,** 6932–6944

70. Levine, E. M., Roelink, H., Turner, J., and Reh, T. A. (1997) Sonic hedgehog promotes rod photoreceptor differentiation in mammalian retinal cells in vitro. *J. Neurosci.* **17,** 6277–6288
71. Karner, C. M., Das, A., Ma, Z. D., Self, M., Chen, C., Lum, L., Oliver, G., and Carroll, T. J. (2011) Canonical Wnt9b signaling balances progenitor cell expansion and differentiation during kidney development. *Development* **138,** 1247–1257
72. Karner, C. M., Chirumamilla, R., Aoki, S., Igarashi, P., Wallingford, J. B., and Carroll, T. J. (2009) Wnt9b signaling regulates planar cell polarity and kidney tubule morphogenesis. *Nat. Genet.* **41,** 793–U746
73. Haynes, T., Gutierrez, C., Aycinena, J. C., Tsonis, P. A., and Del Rio-Tsonis, K. (2007) BMP signaling mediates stem/progenitor cell-induced retina regeneration. *Proc. Natl. Acad. Sci. U. S. A.* **104,** 20380–20385
74. Murali, D., Deng, C. X., and Furuta, Y. (2005) Distinct developmental programs that require different levels of Bmp signaling during mouse retinal development. *Dev. Biol.* **283,** 671–671
75. Caberoy, N. B., Zhou, Y., and Li, W. (2011) Tubby and tubby-like protein 1 are new MerTK ligands for phagocytosis. *EMBO J.* **29,** 3898–3910
76. Vance, J. E., and Steenbergen, R. (2005) Metabolism and functions of phosphatidylserine. *Prog. Lipid Res.* **44,** 207–234
77. Yeung, T., Heit, B., Dubuisson, J. F., Fairn, G. D., Chiu, B., Inman, R., Kapus, A., Swanson, M., and Grinstein, S. (2009) Contribution of phosphatidylserine to membrane surface charge and protein targeting during phagosome maturation. *J. Cell Biol.* **185,** 917–928
78. Yeung, T., Gilbert, G. E., Shi, J., Silvius, J., Kapus, A., and Grinstein, S. (2008) Membrane phosphatidylserine regulates surface charge and protein localization. *Science* **319,** 210–213
79. Opdenkamp, J. A. F. (1979) Lipid asymmetry in membranes. *Ann. Rev. Biochem.* **48,** 47–71
80. Yeung, T., Terebiznik, M., Yu, L., Silvius, J., Abidi, W. M., Philips, M., Levine, T., Kapus, A., and Grinstein, S. (2006) Receptor activation alters inner surface potential during phagocytosis. *Science* **313,** 347–351
81. Raynal, P., and Pollard, H. B. (1994) Annexins—the problem of assessing the biological role for a gene family of multifunctional calcium-binding and phospholipid-binding proteins. *Biochim. Biophys. Acta Rev. Biomembranes* **1197,** 63–93
82. Mollema, N., and Haider, N. B. (2010) Focus on Molecules: Nuclear hormone receptor Nr2e3: Impact on retinal development and disease. *Exp. Eye Res.* **91,** 116–117
83. Daniele, L. L., Lillo, C., Lyubarsky, A. L., Nikonov, S. S., Philp, N., Mears, A. J., Swaroop, A., Williams, D. S., and Pugh, E. N. (2005) Cone-like morphological, molecular, and electrophysiological features of the photoreceptors of the Nrl knockout mouse. *Invest. Ophthalmol. Vis. Sci.* **46,** 2156–2167
84. Farjo, R., Skaggs, J. S., Nagel, B. A., Quiambao, A. B., Nash, Z. A., Fliesler, S. J., and Naash, M. I. (2006) Retention of function without normal disc morphogenesis occurs in cone but not rod photoreceptors. *J. Cell Biol.* **173,** 59–68
85. Jadhav, A. P., Cho, S. H., and Cepko, C. L. (2006) Notch activity permits retinal cells to progress through multiple progenitor states and acquire a stem cell property. *Proc. Natl. Acad. Sci. U. S. A.* **103,** 18998–19003
86. Nelson, B. R., Hartman, B. H., Georgi, S. A., Lan, M. S., and Reh, T. A. (2007) Transient inactivation of Notch signaling synchronizes differentiation of neural progenitor cells. *Dev. Biol.* **304,** 479–498
87. Wang, Y. P., Dakubo, G., Howley, P., Campsall, K. D., Mazarolle, C. J., Shiga, S. A., Lewis, P. M., McMahon, A. P., and Wallace, V. A. (2002) Development of normal retinal organization depends on Sonic hedgehog signaling from ganglion cells. *Nat. Neurosci.* **5,** 831–832
88. Wang, Y. P., Dakubo, G. D., Thurig, S., Mazerolle, C. J., and Wallace, V. A. (2005) Retinal ganglion cell-derived sonic hedgehog locally controls proliferation and the timing of RGC development in the embryonic mouse retina. *Development* **132,** 5103–5113
89. Conte, I., Marco-Ferreres, R., Beccari, L., Cisneros, E., Ruiz, J. M., Tabanera, N., and Bovolenta, P. (2010) Proper differentiation of photoreceptors and amacrine cells depends on a regulatory loop between NeuroD and Six6. *Development* **137,** 2307–2317
90. Alfano, G., Vitiello, C., Caccioppoli, C., Caramico, T., Carola, A., Szego, M. J., McInnes, R. R., Auricchio, A., and Banfi, S. (2005) Natural antisense transcripts associated with genes involved in eye development. *Hum. Mol. Genet.* **14,** 913–923
91. Coleman, J. A., Kwok, M. C., and Molday, R. S. (2009) Localization, purification, and functional reconstitution of the P4-ATPase Atp8a2, a phosphatidylserine flippase in photoreceptor disc membranes. *J. Biol. Chem.* **284,** 32670–32679
92. Webber, A. L., Hodor, P., Thut, C. J., Vogt, T. F., Zhang, T., Holder, D. J., and Petrukhin, K. (2008) Dual role of Nr2e3 in photoreceptor development and maintenance. *Exp. Eye Res.* **87,** 35–48
93. Chen, J. C., and Nathans, J. (2007) Genetic ablation of cone photoreceptors eliminates retinal folds in the retinal degeneration 7 (rd7) mouse. *Invest. Ophthalmol. Vis. Sci.* **48,** 2799–2805
94. D'Cruz, P. M., Yasumura, D., Weir, J., Matthes, M. T., Abderrahim, H., LaVail, M. M., and Vollrath, D. (2000) Mutation of the receptor tyrosine kinase gene Mertk in the retinal dystrophic RCS rat. *Hum. Mol. Genet.* **9,** 645–651
95. Duncan, J. L., LaVail, M. M., Yasumura, D., Matthes, M. T., Yang, H. D., Trautmann, N., Chappelow, A. V., Feng, W., Earp, H. S., Matsushima, G. K., and Vollrath, D. (2003) An RCS-like retinal dystrophy phenotype in Mer knockout mice. *Invest. Ophthalmol. Vis. Sci.* **44,** 826–838
96. Mortazavi, A., Williams, B. A., McCue, K., Schaeffer, L., and Wold, B. (2008) Mapping and quantifying mammalian transcriptomes by RNA-Seq. *Nat. Methods* **5,** 621–628
97. Ashburner, M., Ball, C. A., Blake, J. A., Botstein, D., Butler, H., Cherry, J. M., Davis, A. P., Dolinski, K., Dwight, S. S., Eppig, J. T., Harris, M. A., Hill, D. P., Issel-Tarver, L., Kasarskis, A., Lewis, S., Matese, J. C., Richardson, J. E., Ringwald, M., Rubin, G. M., Sherlock, G., and Consortium, G. O. (2000) Gene ontology: tool for the unification of biology. *Nat. Genet.* **25,** 25–29
98. Kendziorski, C., Irizarry, R. A., Chen, K. S., Haag, J. D., and Gould, M. N. (2005) On the utility of pooling biological samples in microarray experiments. *Proc. Natl. Acad. Sci. U. S. A.* **102,** 4252–4257

Received for publication April 25, 2011.
Accepted for publication May 26, 2011.